American Journal of Geospatial Technology (AJGT)

ISSN: 2833-8006 (ONLINE)

VOLUME 4 ISSUE 1 (2025)

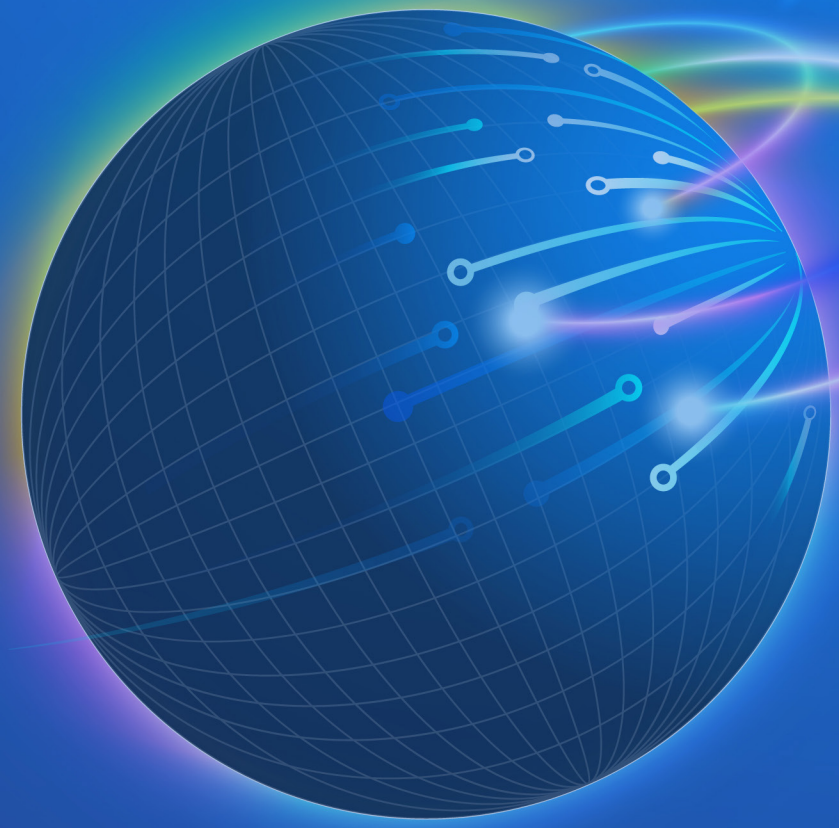

PUBLISHED BY
E-PALLI PUBLISHERS, DELAWARE, USA

American Journal of Geospatial Technology (AJGT)

Volume 4 Issue 1, Year 2025
ISSN: 2833-8006 (Online)
DOI: https://doi.org/10.54536/ajgt.v4i1.2472
https://journals.e-palli.com/home/index.php/ajgt

The Effect of Micrite Content on the Geophysical Properties of Reservoir Carbonate Rocks

Najeeb S. Aladwani[1*], Laurence J.[2], Ismael Himar Falcon-Suarez[2], Angus I. Best[2]

Article Information

Received: April 01, 2024

Accepted: April 29, 2024

Published: February 14, 2025

Keywords

Attenuation, Elastic Wave Velocity, Electrical Resistivity, Micrite Content, Reservoir Carbonate

ABSTRACT

Carbonate rocks have a significant economic value as water and hydrocarbon reservoirs and are essential elements for concrete and buildings. This study selected a total of 36 carbonate rock samples, which were tested in the lab for electrical resistivity at 80 Hz, primary and secondary ultrasonic wave velocity, and attenuation. Therefore, to understand the role of microcrystalline calcite (micrite) on the geophysical properties, this study has proposed a new systematic method by using image analysis techniques to quantify micrite and microstructural parameters such as macro porosity, solid grains, microporous micrite (porosity within micrite), and calcite crystals (sparry calcite). The study findings suggest that porosity and permeability have U-shape trends as a function of micrite content due to leaching processes. Thus, higher micrite content causes the elastic wave velocities to increase, making the rock stiffer. When a dual porosity effect is present, the attenuation exhibits two peaks, and is at its highest with micrite content. With minimal values between 10% and 30% of micrite content due to maximal porosity, the apparent formation factor exhibits a U-shape trend with micrite content; as a result, the electrolyte conductivity is high. We concluded that knowledge of micrite content and macro-porosity is of paramount importance to interpret and model the geophysical parameters and to develop a rock physics model.

INTRODUCTION

Carbonate rocks are major underground reservoirs of hydrocarbons and water (Chilingar *et al.*, 1967) as well as the primary supply of cement for concrete and buildings (Grasby & Betcher, 2002; Hawkins *et al.*, 1996). Understanding the physical characteristics of carbonates, particularly the impact of microstructures, is therefore relevant to many different specialized domains, such as rock physics, hydrology, geotechnical engineering, and tectonics, and is critical for better characterizing reservoir resources. Carbonate rocks have complicated geochemical, textural, and petrophysical features (most critically for reservoir rocks, porosity and permeability), which derive from their geological genesis (by bi oclasts, ooids, and so on) and subsequent diagenetic processes that frequently alter their mineralogy and pore networks. There is a growing body of literature that recognises the microstructural complexity of carbonates and the factors that control elastic wave velocities (both Primary, or P-wave, and Secondary, or S- wave) and the fluid transport properties, porosity and permeability. Recently, the researcher's interest has increased in the contribution of microcrystalline calcite, i.e., micrite, to the microstructural configuration of carbonate rocks (Cantrell & Hagerty, 1999; Husseiny & Vanorio, 2015; Lambert *et al.*, 2006), and its effect on elastic wave properties (Fournier & Borgomano, 2009; Husseiny & Vanorio, 2015; Vanorio & Mavko, 2011). In reservoir sandstones, the scatter often seen in the velocity-porosity relation is frequently attributed to the amount of clay content in the rock (Han, 1986; Kowallis *et al.*, 1984; D. Marion, 1992); indeed, volumetric clay content is a second order control on velocity after porosity. Here, we explore the hypothesis that microcrystalline calcite (micrite) in carbonate rocks has a similar influence to clay in sandstones on elastic wave velocity.

Micrite content can be dependent on the energy level of the depositional environment and is used for petrographic and textural classification of carbonates (Dunham, 1962; Folk, 1959). The micrite is a result of diagenesis, which prompts the recrystallisation of previous rock constituents, calcite and aragonite mud, for instance as stated by (Lambert *et al.*, 2006). The particles gathered with microcrystalline calcite usually have a size between 1 and 4 μm, similar to clay. As a result, they are probably to blame for carbonates' micro porosity (Cantrell & Hagerty, 1999; Vanorio & Mavko, 2011).

The advancement of digital image analysis techniques has revitalised the way that modern petrographic analysis is performed (Hamilton, 2010; Michael Denis Higgins, 2006). Textural measurements such as shape, size, and sorting of crystals or grains can be quickly and accurately acquired on 2D rock images (Michael D Higgins & Roberge, 2007; Dougal A Jerram *et al.*, 2009), removing ambiguity in classifications. Images are typically obtained from petrographic thin sections as transmitted light photographs or SEM backscatter images. Three-dimensional (3D) rock textures of natural rock samples images can be captured and analysed through the application of serial sectioning and X-ray computed

[1] Department of Earth and Environmental Sciences, Faculty of Science, Kuwait University, Kuwait, Safat 13060, Kuwait
[2] National Oceanography Centre, University of Southampton Waterfront Campus, European Way, Southampton, SO14 3ZH, UK
[3] Ocean & Earth Science, University of Southampton Waterfront Campus, European Way, Southampton, SO14 3ZH, UK
[*] Corresponding author's e-mail: aladwaninajeeb@outlook.com

tomography scan analysis (D A Jerram & Higgins, 2007; Dougal A Jerram *et al.*, 2009).

ImageJ (Rasband, 1997) is a widely used image-processing software that was developed by the National Institutes of Health (NIH) in the USA. Image analysis techniques have major advantages over conventional methods (e.g., manual point counting and visual descriptions), such as the potential to automate and increase the capacity of standard measurements with more speed, precision and accuracy than traditional methods. For example, the measuring of rock porosity from thin sections impregnated with blue epoxy resin is a common method in geosciences and is usually conducted by point counting (Grove & Jerram 2011). However, point counting of thin sections requires special equipment, is laborious and very slow, and human error must be considered. By contrast, digital image analysis is far superior as it measures millions of points in the sample with speed, precision and accuracy; therefore, it presents far superior datasets (Ceia *et al.*, 2017; Haines *et al.*, 2015; Hamilton, 2010).

The objectives of this study were to (1) suggest and establish a method that allows us to extract key sedimentology-related parameters of interest from carbonate reservoir rock samples, such as the volumetric microcrystalline calcite (micrite) content and macro porosity and (2) to investigate the effect of microcrystalline calcite (micrite) on important reservoir petrophysical (porosity, permeability) and geophysical (elastic wave velocity and attenuation, and electrical resistivity) properties.

Although a thin section is a two dimensional slice through a three-dimensional rock, it was shown by Chayes (1956) that the relative areas of the constituents of the sample are equivalent to their relative volumes (Marks, 1994).

Description of Rocks

This study selected 36 carbonate rocks, comprising 24 carbonate samples dataset from (North *et al.*, 2013) *et al.* (2012). Eleven oolitic limestone samples were taken from three core samples of bio clastic oolitic limestone from the Jurassic Purbeck formation of southern England, and thirteen dolomite samples were taken from a single core sample of a microbial-laminated dolo-mudstone from the Rotweil formation of the Southern German basin (Laurence (North *et al.*, 2013) *et al.*, 2013).

A suite of 12 new limestone samples was chosen to expand the dataset of (North *et al.*, 2013) *et al.* (2012). Eleven samples were from wells in Hampshire's Wealden Basin in southern England, comprising two samples from Horndean lA (SU 71541260), six samples from Homdean 4 (SU 66301346), three samples from Humbly Grove-3 (SU 7054 4530) and one sample from Calub 1 in the Ogaden Basin, south-eastern Ethiopia (Berhanu, 1994).

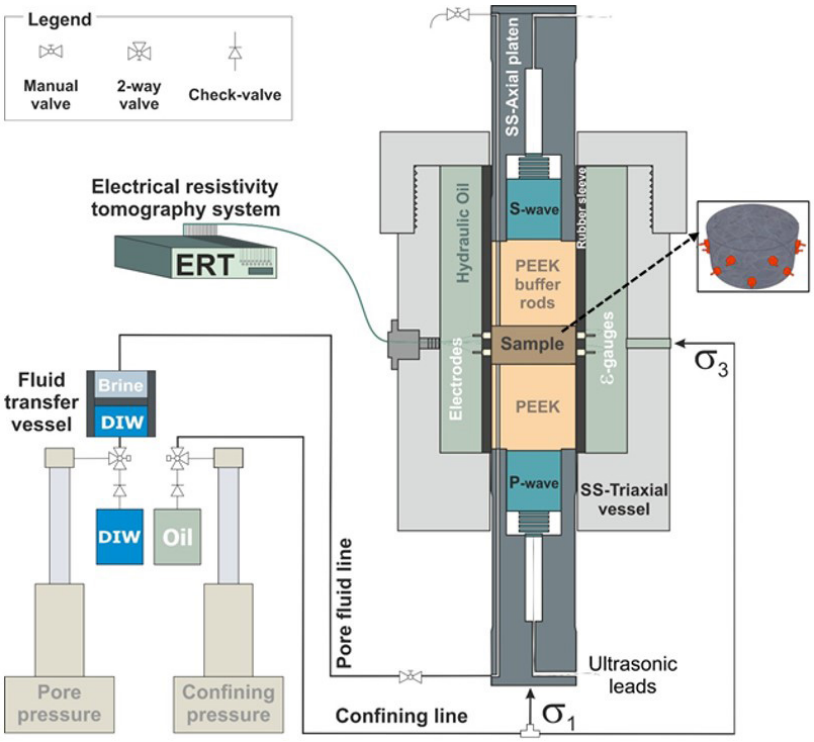

Figure 1: Schematic diagram of the experimental setup, also showing the arrangement of electrodes around the rock sample. Scales are approximate (sample width is 5 cm). After Falcon-Suarez *et al.* (2017), North *et al.* (2013).

The Wealden Basin, southern England, comprises several formations, for example, the Hesters Copse Formation and the Great Oolite. The Hesters Copse formation is divided into a wackestone unit (oolitic and bioclastic), a dolomite unit (calcareous dolomite) and a basal sandstone unit (fine-grained calcareous sandstone). Next, the dominant component in the Great Oolite formation is oolitic, skeletal and oncolytic grain stones

and pack stones (Sellwood, Shepherd, Evans, & James, 1989). Overall, diagenetic processes in these rocks are compaction, dissolution and late cementation (Berhanu, 1994). The limestones from the Ogaden Basin belong to the Hamanlei Formation. The Hamanlei Formation is composed of several limestone facies like grainstones (peloidal, oolitic and skeletal) to mudstones, dolostones and evaporates (Berhanu, 1994).

A collection of more than one hundred rock samples which had previously been analyzed in a lab using an ultrasonic pulse-echo device were used to choose the samples (Berhanu, 1994b). The best samples for this investigation were chosen using the findings of petrophysical studies, which included porosity, permeability, ultrasonic velocity, and attenuation. For this study, new resistivity measurements are essential because they enable the examination of joint elastic-electrical properties. Additionally, new ultrasound measurements are crucial because they provide a cross-check on the samples to determine whether they have changed since the initial petrographic and ultrasonic property measurements.

Thin-Sections Description

The thin-section 1 was taken in plane-polarised light of sample RS08A, a limestone rock (grainstone according to Dunham classification scheme). The field of view is mostly occupied by grains of oolite, pellods and some shell fragments, and the cement by large calcite crystals with perfect rhombohedral cleavage. Most crystals show at least one good cleavage. The thin-section 1 is an example of a grain-supported (GS) microstructural texture (micrite content less than 10%) with sparry cement and grains forming tight arrangements of mosaic-like texture.

The thin-section 2 was taken in crossed-polarised light of sample RS08B, a limestone rock (grainstone according to Dunham classification scheme). The field of view is occupied mostly by grains of oolite, pelloids and some shell fragments. The thin section was stained by the dye Alizarin Red S so both macro pores and calcite crystal show a yellowish colour, but in crossed-polarised light, the macro pores turn black, as shown in thin sections 2 and 3. Under crossed-polarised light, the interference colour for calcite crystals in a lower photograph in Figure 1, Thin-section 2, can be seen to be of very high order birefringence (the thin-section might be a slightly less than normal 0.03 mm in thickness since in sections of standard thickness the interference colour produced is a high-order white (Mackenzie *et al.*, 1980).

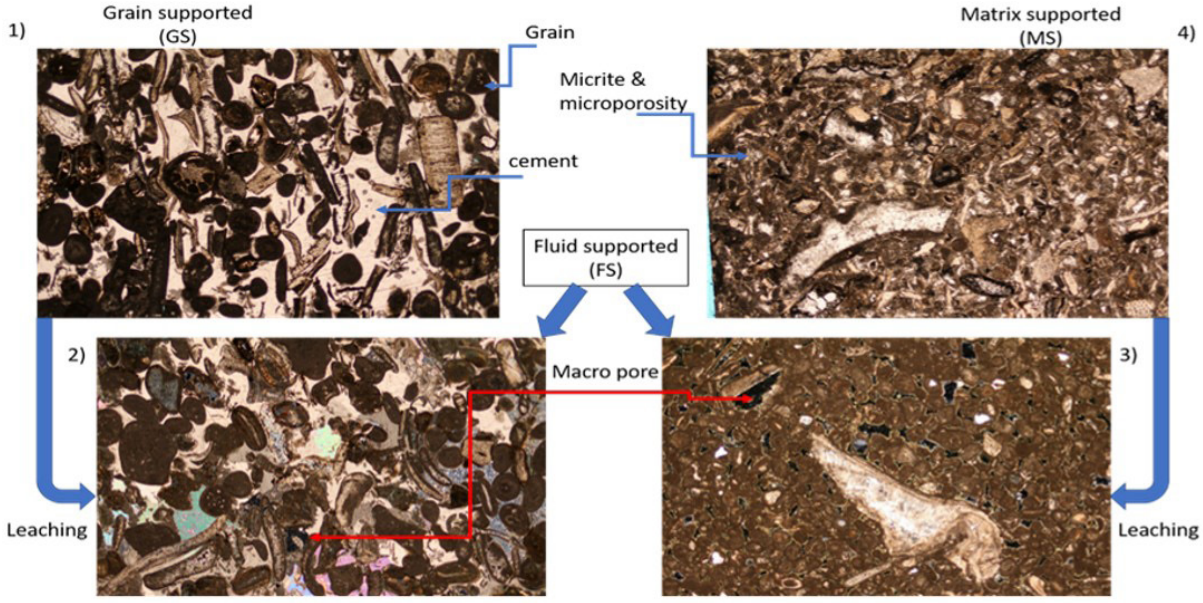

Figure 2: Thin selections optical images under the microscope. 1) The thin-section taken in plane-polarized light and it is RS08A, limestone rock (grainstone according to Dunham classification scheme). (2) The thin-section taken in plane-polarized light and it is RS08B, limestone rock (grainstone according to Dunham classification scheme). 3) The thin-section taken in plane-polarized light and it is Base Bed 3, limestone rock (wackestone according to Dunham classification scheme). 4) The thin-section taken in plane-polarized light and it is S-39446, limestone rock (wackestone according to Dunham classification scheme).

Both the limestone and dolomite may show a twinkling effect, which is caused by some minerals like calcite and dolomite crystals showing a marked change in relief when the microscope stage is rotated (Anthony E Adams *et al.*, 2017; Mackenzie, W. S/ Guilford, 1980). The thin-section 2 is an example of a fluid-supported (FS) microstructural texture with a slightly higher number of macro pores (black colour) with sparry cement (micrite content less than 10%) and grains forming tight arrangements of a mosaic-like texture.

Whereas, the thin-section 3 was taken in crossed-polarised light of sample Base Bed 3, a limestone rock (wackestone

according to Dunham classification scheme). The field of view is occupied mostly by grains of oolite, pelloids and some shell fragments and micrite matrix. The thin-section 3 is an example of a fluid-supported (FS) microstructural texture with a slightly higher number of macro pores (black colour). The micrite matrix, which is mainly constituted of aggregates of rounded, micrite crystals, confers a stiff and tight texture to the rock (Vanorio & Mavko, 2011).

Under plane-polarized light, sample S-39446-a limestone rock classified as wackestone under the Dunham categorization scheme-was examined in thin-section 4. The majority of the objects in the view's field were oolite grains, pelloids, micrite matrix, and a few shards of shell. An illustration of a matrix supported (MS) microstructural texture is thin-section 4. The micrite matrix, which is mostly made up of clusters of spherical micrite crystals, gives the rock a tight, hard feel (Vanorio & Mavko, 2011).

Table 1: Rock composition (from thin polished section)

Sample name (WELL-DEPTH)	Fm.	Facies	Rock composition from thin section (%)									
			Grain						Cement		Matrix (Mic.)	Mean Grain dian (μ m)
			Ooid	Inel	Skel.	Cal.	Qz.	Dol	Mic	Non mic		
Well:H1A												
S-39400	Great Oolite	WKST	23	3	12	0	0	0	9	0	50	668
S-39415		WKST	46.4	0	3.1	0	0	0	17.9	0	15.9	480
WELL:H4												
S-39433	Great Oolite	PKST	41.3	0	7.7	1.2	0	0	39.4	0	2.1	692
S-39437		GRST	30.4	0	4.3	0	0	0	36.5	0.3	7	423
S-39438		GRST	34.9	0	22.1	13.9	0	0	16.1	0	0.6	787
S-39440		GRST	34.1	0	18.7	0	0	0	35.3	0	0.9	205
S-39446		WKST	24.4	0	24.4	2.8	0	0	16.9	0	24.4	603
S-39448		PKST	27.4	0	21	4.6	0	0	30	0	7.1	930
well: HG3												
S-39454	HC	MST	0	0	0	0	43.7	7	42	0	5.3	68
S-39456		MST	0	0	0.3	1.7	33.7	2.6	37.8	0	10.4	98
S-39457		PKST	6.2	3.8	20.9	3.4	0.3	29.9	27.1	0	7.2	940

Note: GO=Great Oolite, HC=Hester's Copse, GRST=Grainstone, PKST=Packstone, WKST=Wackestone and MST=Mudstone). This table was adapted from (Berhanu, 1994)

MATERIALS AND METHODS

Experimental procedure

Every sample has been prepared using the normal procedures outlined in (McCann, 1992; Han, 2011b). The samples were cut to a length of 2 cm, having their two end faces ground parallel and flat to within ± 0.01 mm. The samples were cleaned and cored as cylindrical plugs with a 5 cm diameter. After placing them in an oven set at 40 °C for three days, the samples were dried. After the samples had been cleaned and dried, they were evaluated, dimensions were recorded, and for three days they were submerged in 35g/l of brine at a pressure of 7 MPa. Subsequently, the saturated samples were placed in a brine-filled tank and swiftly transferred into the high-pressure rig for electrical and ultrasonic measurements.

For carbonate rocks, the pore fluid pressure was kept at 5 MPa. The geophysical parameters P- and S-wave velocity and attenuation, as well as electrical resistivity, were measured successively for each sample at each effective pressure of 50, 40, 30, 20, and 10 MPa. The pressure was given 30 minutes to equilibrate before measurements were started. The temperature and relative humidity in the laboratory were maintained at 19 ± 1°C and 50 ± 1%, respectively.

Joint Ultrasound and Electrical Resistivity Tomography (ERT) Rig

At frequencies ranging from 400 kHz to 800 kHz, P- and S-wave velocities (Vp, Vs) and attenuations (Qp-1, Qs-1) were measured using the ultrasonic pulse-echo technique (Winkler, 1982; McCann, 1992). Researchers employed a dual P- and S-wave transducer/receiver with measurement accuracy of ± 0.3% and ± 0.2 dB/cm for the velocity and attenuation coefficient, respectively (Best, 1992). Figure 1 shows the high-pressure rig, and in accordance with (North *et al.*, 2013), the sample assembly was modified for resistivity tomography measurements.

The sample was encircled by a rubber sleeve that held 16 tetrapolar stainless steel electrodes spaced radially into two rings for the purpose of measuring the electrical

resistivity tomography (Figure 1). The electrodes provided a resistivity measurement error under typical working circumstances of < 0.1% at frequencies 1 - 500 Hz, with a sample electrical resistivity range of 1 - 100 Ohm m. The electrodes permitted current injection and boundary voltage probing in many permutations.

Estimation of Microstructural Parameters

While experimentation, the carbonate sample microstructure was divided into five main parameters: macro porosity, solid grains, microporous micrite (porosity within micrite), micrite content (micrite excluding any microporosity), and calcite crystals (sparry calcite). Microporous micrite has a lower density than solid calcite grains due to the presence of microporosity. As a result, the microporosity and solid micrite grains can be separated according to the grey scale intensity contrast in petrographic images. Consequently, image processing techniques were also used that were suggested by Grove and Jerram (2011) and Vanorio and Mavko (2011) to quantify the five microstructural parameters from optical microphotographs of the carbonates and dolomite samples. However, in practice, this was only feasible for dolomite samples because the intensity contrast was insufficient for the carbonate samples. The study used Fuji/ImageJ software. Additionally, the study presented an approach to estimate the uncertainty associated with the quantified parameters.

Estimation of Parameters From Optical Microscopy

The petrographic thin sections were blue resin-impregnated to facilitate observation of porosity from optical microscopy images, and the dolomite samples thin-sections were stained by the dye Alizarin Red S, used here to differentiate calcite and dolomite (dolomite shows original clear stain colour, while calcite shows a pink tored–brown when stained). The dyes are dissolved in a weak acid solution as dolomite does not react with cold dilute acid, whereas calcite does. During the practical experimentation, basically, two stages to process the images were used and five different textural classes. To illustrate the process, it was suitable to refer an example images in Figures 4.2 – 4.7 and the microstructural elements outlined in Table 4.2.

Table 4.2: Relative image intensity levels of each microstructural element, and symbols used in text

Microstructural element	Symbol	Image intensity	Grey levels Min/Max
Macro porosity	ϕmacro	Black	0-40 (± 20)
Ooids, pelloids and shell fragments	F bio	Dark grey	40-90 (± 20)
Micrite	Micrite	Grey	90-160 (± 20)
Calcite, sparite	F calcite	Light grey	160-255 (± 20)
Microporosity in dolomite	ϕmicro	White	120-225 (± 20)

However, figure 2 shows a flowchart for the key operations used to extract the relevant measurement. Digital image acquisition was achieved using a NIKON D5600 DSLR Camera attached to a microscope to acquire a digital image directly from the thin section. The image was acquired with low magnification (5X zoom) in an optical microscope to capture a large area so that it will be representative of the rock (Croizé *et al.*, 2010; Fournier & Borgomano, 2009; Lambert *et al.*, 2006; Saxena, Hofmann, *et al.*, 2017). Grove & Jerram (2011) pointed out that some of the images they acquired at low magnification had distortion toward the edges of the frame (darker than the rest of the frame). Still, the author did not observe this in the low-magnification images.

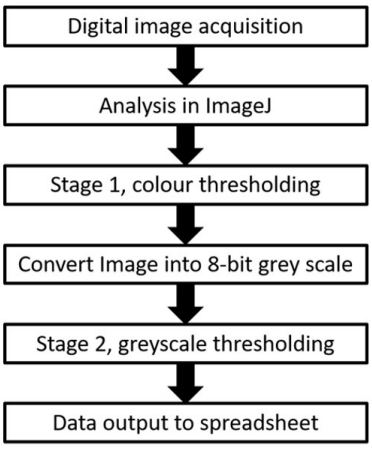

A total of five different locations were captured from the thin section, and each optical microscopy image was used to estimate the microstructural parameters of interest. It was determined that the overall microstructural parameters for the rock by averaging the values obtained from all five images. Figure 3 shows the workflow that was used to estimate the microstructural parameters. The first stage was colour thresholding the images to indicate the macro porosity, which has a blue colour for blue resin-impregnated thin sections, as shown in Figures 3A & B, and appears yellow to black for thin sections stained by Alizarin Red S dye in Figure 3C. For example, fenestral porosity in a carbonate rock is pore space larger than the normal grain-supported spaces, and it can be a different size or shape depending on its origin (see Figure 3 C).

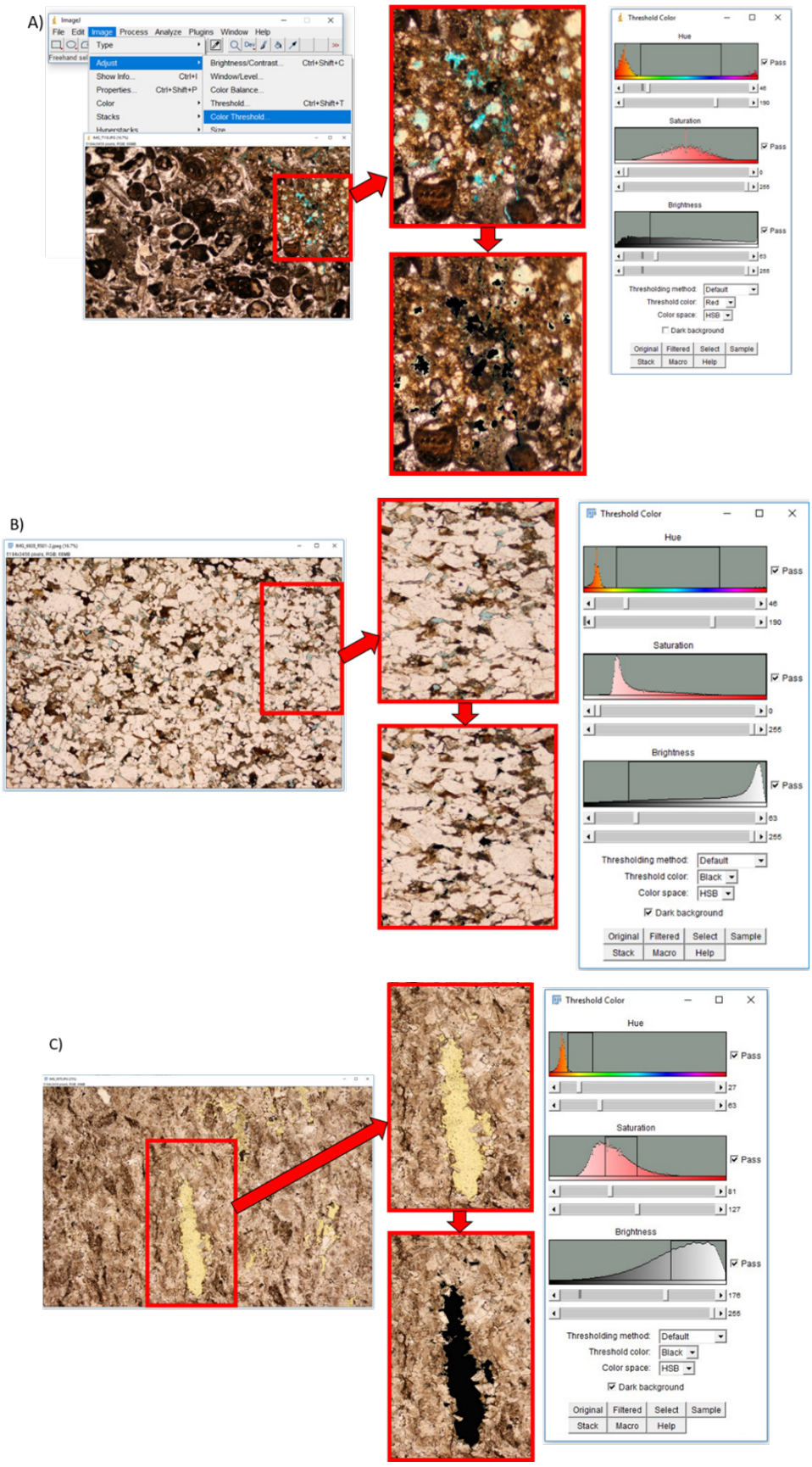

Figure 3: Workflow using stage1, colour thresholding within ImageJ to convert the blue colour to black. Screenshots are shown for key operations. A) Segmentation of a thin section optical image (from sample S-39400, an oolitic limestone) under the transmitted light microscope. B) Segmentation of a thin section optical image (from sample RS01-2, a sparry calcite) under the transmitted light microscope. C) Segmentation of a thin section optical image (from sample GRN 2 a sparry calcite) under the transmitted light microscope.

Fenestrae with an elongated shape might be due to entrapment of fluid in a sediment during desiccation (A E Adams *et al.*, 1984). Using ImageJ, 24-bit colour images are thresholded using an 8-bit colour conversion tool (image>Type>8-Bit colour) set to 256 colours. Then, converted the blue/yellow colour to black. One of the drawbacks of using grey-intensity thresholding is that the macro porosity in blue resin-impregnated and Alizarin Red S dye-stained thin sections changes colour to grey, giving a low contrast between macro porosity and micrite aggregates, making it difficult to segment. This can be avoided by changing the colour of the macro porosity from blue /yellow to black, so it can be easily distinguished during the subsequent grey-scale intensity thresholding. The image was then converted to a grey-scale, as shown in Figure 4A.

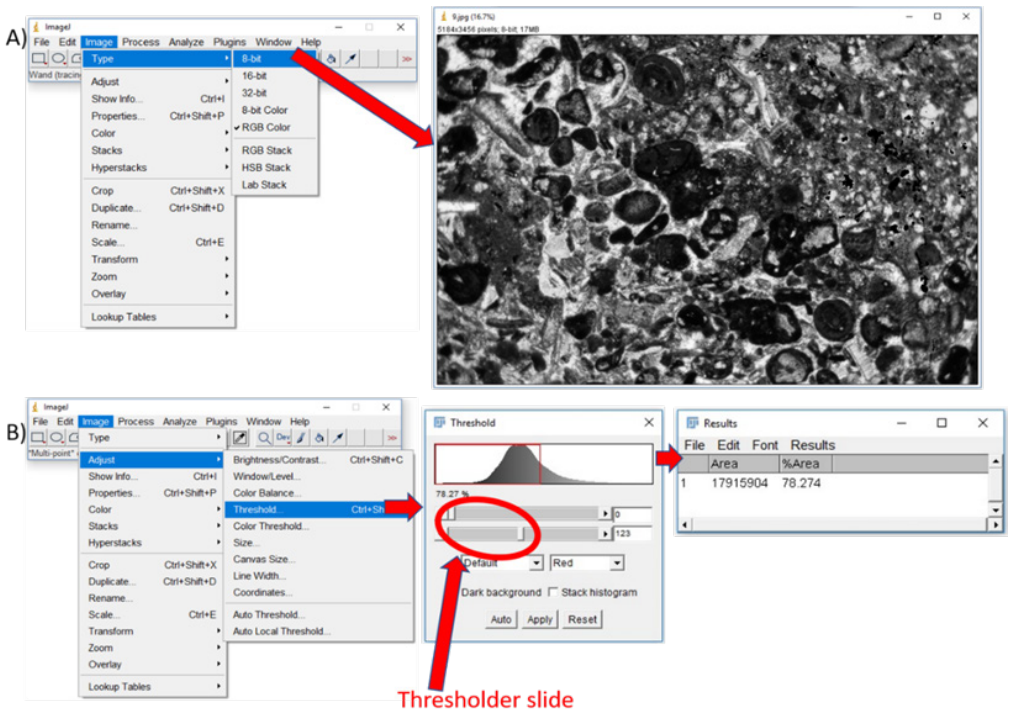

Figure 4: Workflow using stage2, greyscale thresholding within ImageJ. Screenshots are shown for key operations. A) image convert to 8-bit grey intensity. B) Shows greyscale thresholding the image and thresholder slide used to choose the greys intensity for microstructural parameters and the results

The second stage of the workflow was to use grey-scale thresholding to segment the images. Table 4.2 shows the different grey-scale intensities for the variety of allochem type clasts; for example, bioclasts and coated grains (ooids), calcite (sparite), micrite, micro porosity and macro porosity. This diversity in the intensity response allowed us to segment the picture and obtain five different distinct classes. It was judiciously selected a value for thresholding based on a grey-scale intensity and geology knowledge to segment the image. After that, it can be calculated the fraction of the classes associated with the grey-scale intensities below the threshold. A two-step segmentation scheme (i.e., two threshold values) allowed to obtain the microstructural parameters as follows: (A) the first threshold separates the macro porosity (i.e., black regions in optical microscope image) from the rest of the image, (f1), is given by

$$f1 = \emptyset_{macro,} \quad (1)$$

Where f1 is the first threshold and $\emptyset_{macro}$ is macroporosity. Thereby calculating the macroporosity (ϕ_{macro}) as illustrated in Figures 5, (A), Figure 6 (A) and 4.7 (A). The second threshold (f2) has a higher grey-intensity value than the first threshold and separates the fbio and macro porosity from the rest of the image, as shown in Figure 5 B f2 is given by

$$f2 = \emptyset_{macro} + f_{bio,} \quad (2)$$

Where f2 is the second threshold and f_{bio} is a fraction of ooids, pelloids and shell fragments. The fraction of calcite crystals (fcalcite) has a light grey colour, so to calculate the sparry calcite only in ImageJ software, it simply reverses the threshold to start from white to black, and the results are added to solid grains (fgrains), see Figure 5C and Figure 6C. $f_{calcite}$ is given by

$$f_{calcite} = f3, \quad (3)$$

where $f_{calcite}$ is the fraction of calcite crystals (sparite), and f3 is the third threshold.

The fraction f_{bio} is given by

$$f_{bio} = f2 - \emptyset_{macro.} \quad (4)$$

The fraction of solid grains f_{grains} is given by

$$f_{grains} = f_{bio} + f3 \ (\ fcalcite) \quad (5)$$

The fraction of micrite aggregate, i.e., solid micrite crystals (fmicrite) + micro porosity (ϕmicro), is given by

$$fmicrite\ aggregate = 100 - (fgrtains + \emptyset_{macro}) \quad (6)$$

The micro-porosity cannot be estimated directly from

optical microscope images due to the low magnification used in the image acquisition. In a low magnification image, the contrast in a grey intensity for the solid micrite crystals and microporosity is too low to be thresholded. Therefore, the micro-porosity was estimated indirectly by subtracting the macro-porosity from the measured helium porosity (ϕ); $\emptyset_{micro}$ is given by

$$\emptyset_{micro} = \emptyset - \emptyset_{macro,} \quad (7)$$

where $\emptyset_{micro}$ is microporosity, $\emptyset$ is measured helium porosity and $\emptyset_{macro}$ is macroporosity. Finally, the micrite content $f_{micrite}$ is given by

$$f_{micrite} = f \text{ micrite aggregate} - \emptyset_{micro} \quad (8)$$

The overall fraction of microstructural parameters for each rock sample was estimated in the five different images and then averaged.

Figures 5 to 7 show examples of the Stage 2 workflow: grey-scale intensity thresholding of the segmentation output separating solid grains' from macro porosity and calcite crystals. Figure 5 is rock sample S-39400, an oolitic limestone (Wackestone).

Figure 5A shows the final segmented image with macro porosity in black. Figure 5B, shows macro porosity and solid grains, which can be recognised in two forms: allochems type clasts such as bioclasts and coated grains (ooids) highlighted in red. Figure 5 C shows the calcite in red colour.

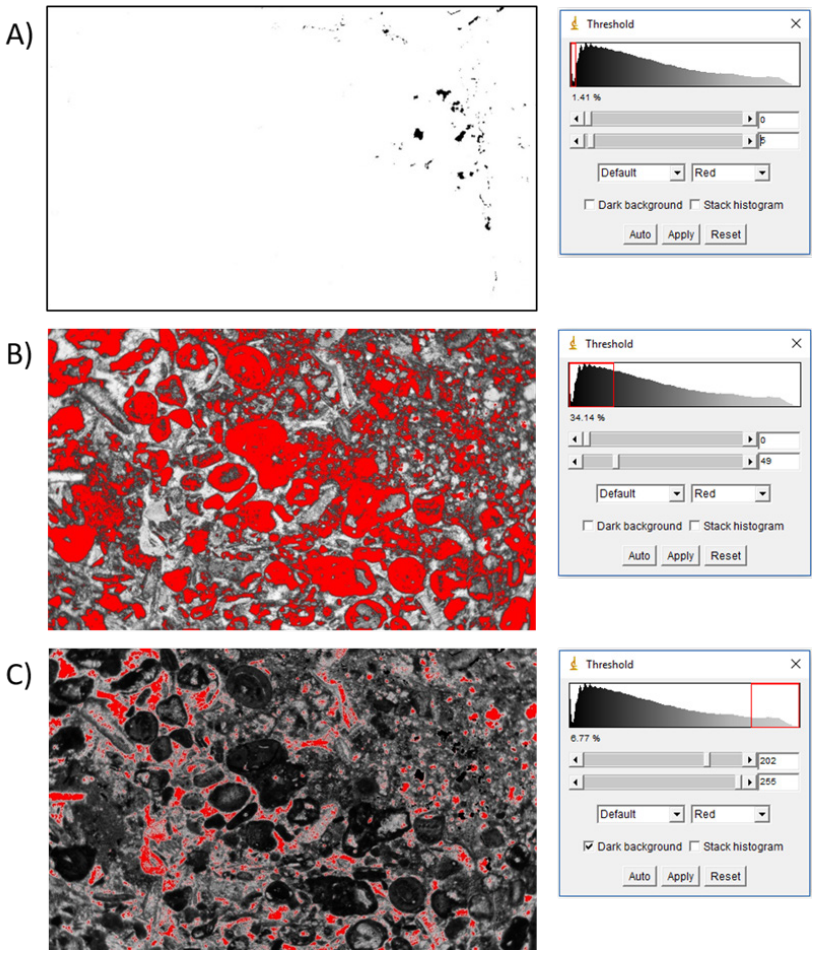

Figure 5: Segmentation of a thin section optical image (from sample S-39400, an oolitic limestone, Wackestone) under the transmitted light microscope. A) The macroporosity is highlighted in black. B) Shows macroporosity and bioclasts and coated grains (ooids) highlighted in red. C) Shows calcite in red colour

Figure 6 shows a sequence of digital images of a thin section microphotograph of sample RS01-2 (pack stone according to Dunham classification scheme). The macro porosity is shown in black in Figure 6 A. This sample comprises entirely sparry calcite without any ooids, so some adjustment has been made for the calculation of microstructural parameters. The first threshold was the macro porosity. The second threshold was macro porosity and micrite aggregate. The micrite aggregate can be calculated by subtracting f1 from f2. The third threshold was calcite. The micro-porosity was calculated using Equation 7.

Figure 7 shows sample ALG1.1, a dolomite rock (microbial-laminated dolo-mudstone according to Dunham classification scheme). Figure 7 A shows the first threshold macro porosity. The second threshold was macro porosity and micrite aggregate. The micrite aggregate can be calculated by subtracting f2 from f1, as shown in Figure 7 B. The third threshold was the microporosity within micrite aggregate, as shown in Figure 7 C.

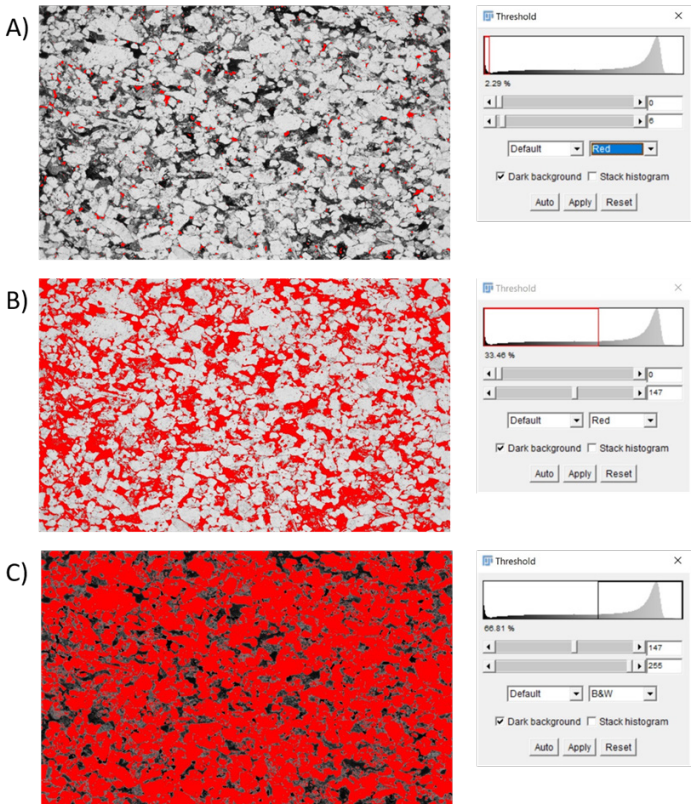

Figure 6: Demonstrating of the first stage segmentation of thin section optical image (Packstone; sample No. RS01-2 under the microscope .A) The macroporosity is highlighted in black. B) Shows macroporosity and micrite highlighted in red. C) Shows calcite in red colour

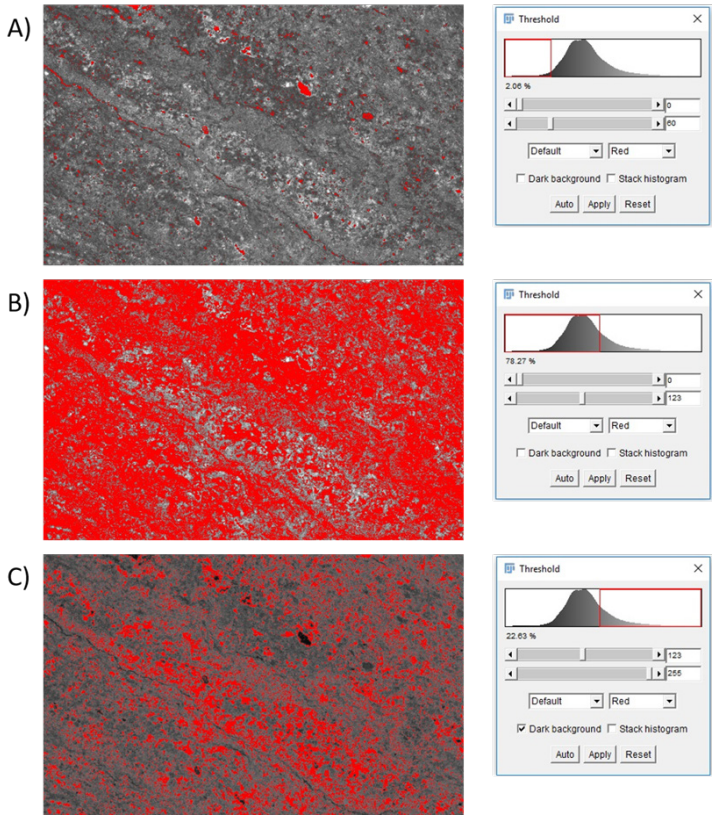

Figure 7: Demonstrating of the segmentation of thin section optical image under the microscope. The sample ALG 1.1 a, dolomite rock (microbially- laminated dolo-mudstone according to Dunham classification scheme). (A) The macroporosity was highlighted with red colour. (B) The micrite aggregate was highlighted in red colour. (d) The micro-porosity was highlighted with red colou

Generally, the workflow is able to distinguish (visually) quite well the different components of calcite grains, macroporosity and micrite aggregate (including micro-porosity). However, it is not possible to resolve the actual micro-porosity associated with the micrite aggregates in limestone samples as micrite consists of clay-size particles (1 - 4 μm); we would need a higher magnification to capture the micro-porosity.

Quantification of Uncertainty Associated with Parameters Estimation

Quantifying the uncertainty related with an estimation of microstructural parameters is important to indicate the reliability of rock-type classifications for theoretical modelling. Table 4-3 shows an example of the uncertainty associated with the picking threshold when pushing the limit of what would be the correct thresholding to see the sensitivity of each parameter. Table 4-3 shows four examples, one from each facies: mudstone, wackestone, packstone and grainstone.

A semi-quantitative estimate of confidence, as a measure of uncertainty, was determined by calculating the estimated percentages of the parameters of interest (macroporosity, oolitic grains, calcite and micrite) for the chosen threshold grey scale value, and for this threshold value plus or minus ten grey scale units. The results in Table 4-3 show the variation in all parameters is less than 6% for all rock types. Thus, the uncertainty associated with the picking threshold is within an acceptable range, and the results still show similar trends for micrite content as a function of porosity, permeability and compressional velocity as the results reported in the literature (Vanorio, 2011; El Husseiny, 2015).

Estimated Parameters and Associated Uncertainty

Figure 8 below shows a comparison between micrite aggregate estimated using digital photomicrographs of thin sections by an optical microscope and that estimated from the point counting method for samples with available data (only 10 samples). The results show that the two techniques, in general, are comparable. Moreover, figure 8 also shows micrite aggregate estimated by two different techniques: by image analysis using ImageJ software and by point counting. The most interesting aspect of this graph is that the two techniques, in general, are comparable for the samples characterised by very low or high microcrystalline calcite with micro-porosity. In contrast, there is a mismatch for the samples with intermediate micrite aggregate (30% - 50%). The vertical bar corresponds to the standard deviation associated with average reported micrite aggregate from optical microscope image technique.

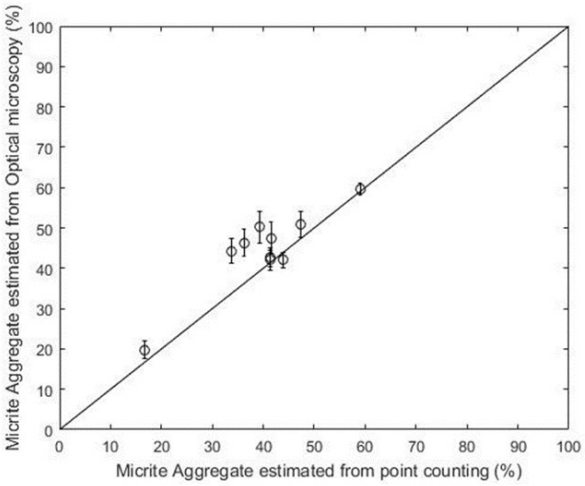

Figure 8: Plot of micrite aggregate (i.e., solid micrite crystals (fmicrite) + micro porosity (ϕmicro) estimated from the optical image under the microscope versus that obtained from point counting

In general, the mismatch might be due to the larger number of data points used in ImageJ image analysis than used in point counting. Equally important, the parameter standard deviations for these samples are relatively high, indicating the samples are more heterogeneous. Therefore, the two techniques are less likely to match. Furthermore, in the next sections, the study also explored the relations between the parameters measured from image analysis, and in particular, the effect of micrite content on reservoir and geophysical properties.

Table 4-3: Semi-quantitative estimate of confidence when using threshold and ± 10 is grey scale values

Samples	Facies	Macroporosity (%)			Oolitic grains (%)			Calcite (%)			Micrite (%)		
		-10	Threshold	+10	-10	Threshold	+10	-10	Threshold	+10	-10	Threshold	+10
ALG1.3	Mudstone	5.09	8.13	12.72	0	0	0	0	0	0	87.28	91.87	94.91
Base Bed 3	Wackstone	0.41	3.31	8.35	53.74	58.63	64.21	4.71	5.81	7.53	28.24	32.25	38.11
S-39457	Packstone	0	1.37	6.88	23.39	25.37	27.92	32.87	42.15	50.21	28.45	31.11	34.72
RS08B	Grainstone	0.33	1.05	5.68	58.2	61.48	64.57	27.01	30.11	33.42	4.26	7.36	10.67

RESULTS AND DISCUSSION

The Effect of Micrite Content on Reservoir Porosity, Permeability and Geophysical Properties

Micrite and Porosity Relationships

Figure 9 shows a cross-plot of the microcrystalline calcite (micrite) and porosity on a log-linear scale for all 21 limestone samples and 15 dolomite samples. For limestones and dolomites in Figure 9, a U-shape was observed where micrite content ranged from 0% to 10%, showing no relationship between micrite content and porosity as a different range of porosity was found between 0% and 10% micrite content.

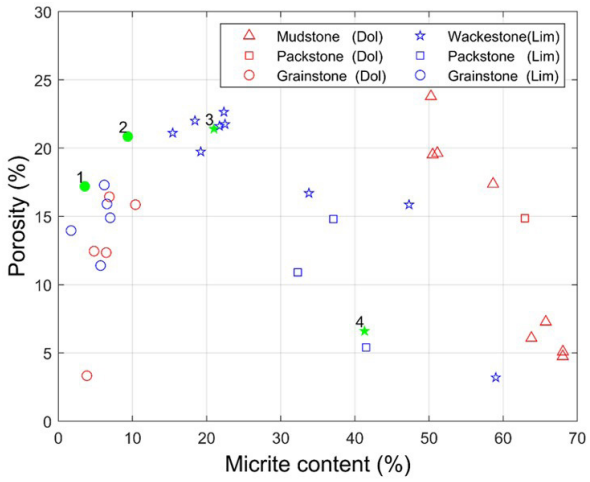

Figure 9: Shows the variation of porosity as a function of micrite content. Red data are the limestone samples, and blue are the dolomite samples. The numbers in black refer to values measured on the samples whose microstructure is shown in Figure 1.

Vanorio and Mavko (2011) showed a similar trend to this study of porosity as a function of micrite content. On the other hand, (Husseiny & Vanorio, 2015; Dominique Marion, 1990) reported an opposite trend of porosity as a function of micrite content. The trend was from synthetic micrite samples that lack macroporosity. Whereas, in our study, and in that of (Vanorio & Mavko, 2011), the samples were from natural carbonate rocks which are inherently populated with macro porosity and, secondary porosity. The presence of secondary porosity can be derived from different diagenetic evolution of porosity in carbonates rocks.

The numbers in black in Figure 9 refer to values measured on the samples whose microstructure is shown in Figure 1. A visual check of the thin sections 1 to 4 in Figure 1 for limestone samples (dolomite samples showing similar microstructures) shows a possible mechanism for the trends in Figure 9 porosity with micrite content.

Thin section 1 in Figure 1 corresponds to sample number 1 in Figure 9, which is sample RS08A (a grain stone according to Dunham classification scheme). Figure 9, Sample 1, represents a grain supported (GS) microstructural texture (micrite content less than 10%) with sparry cement and grains forming tight arrangments of mosaic-like texture. Thin section 2 in Figure 1 corresponds to sample number 2 in Figure 9, which is RS08B (a grain stone according to Dunham classification scheme). Sample 2 represented fluid supported (FS) rock which had a secondary porosity, like vugs, fenestral and moldic porosity.

For limestones and dolomites in Figure 9, porosity starts to increase for micrite content lower than 10%. Thus, a possible mechanism for this behaviour could be diagenesis; for example, as the grains and sparry cement of sample 1 in Figure 9 become corroded and etched around their boundaries, this could result in the textural features seen in, for example, sample 2. The carbonate diagenesis dissolution and leaching process may transform sample 1 grain stone supported texture to evolve toward a fluid-supported texture, as seen in sample 2 in Figure 1.

Thin section 4 in Figure 1 corresponds to sample number 4 in Figure 9, which is S-39446 (wackestone according to Dunham classification scheme). This sample has a matrix-supported (MS) rock microstructure predominantly constituted of aggregates of rounded, microcrystalline calcite (micrite), conferring a stiff and tight texture to the rock. Hence, a significant portion of the total porosity is formed from small, rounded micro-pores of micrite. Thin section 3 in Figure 1 corresponds to sample number 3 in Figure 9, which is Base Bed 3 (wackestone according to Dunham classification scheme). Thin-section 3 shows significant numbers of macropores.

For limestones and dolomites in Figure 9, porosity decreases from the maximum around 10 – 30% micrite as micrite content increases to 70%. The majority of dolomite samples that have micrite content above 30 % were wackestone and pack stone and the dolomite samples were mudstone. A possible mechanism for this behaviour could be diagenesis, illustrated by, for example, as sample 4 textures alter to textures seen in sample 3 in Figure 9; it can be seen that some micrite has been washed out from the intergranular space. The carbonate diagenesis dissolution and leaching process leads to micro-pores becoming more connected, and the development of molds, large vugs and channels, as seen in sample 4 in Figure 1. That is, a matrix supported rock evolves toward a fluid supported rock.

Figure 10 shows the cross-property relation between macro porosity and micrite content. Note that micrite content is inversely proportional to the amount of macro porosity (see equation 1). The micro-porosity in Figure 11 increases as micrite content increases and these data agree with the literature (Baechle *et al.*, 2004; Brigaud *et al.*, 2010; Cantrell & Hagerty, 1999; Eberli *et al.*, 2003; Fournier & Borgomano, 2009; Kazatchenko *et al.*, 2006; Norbisrath *et al.*, 2015; Regnet *et al.*, 2015; Vanorio & Mavko, 2011; Weger *et al.*, 2009).

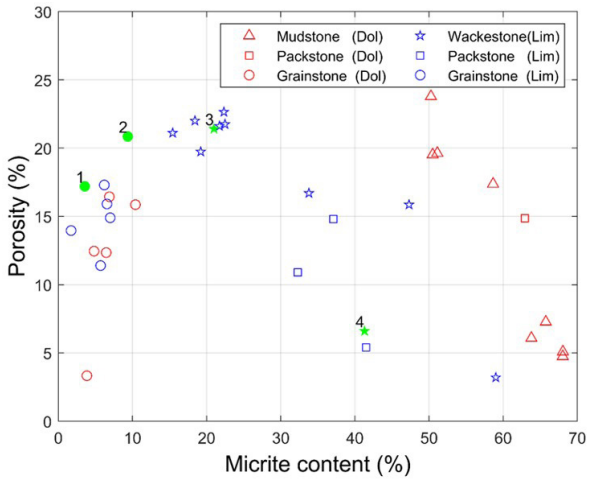

Figure 10: Shows the variation of macroporosity as a function of micrite content. Red data are the limestone samples, and blue are the dolomite samples

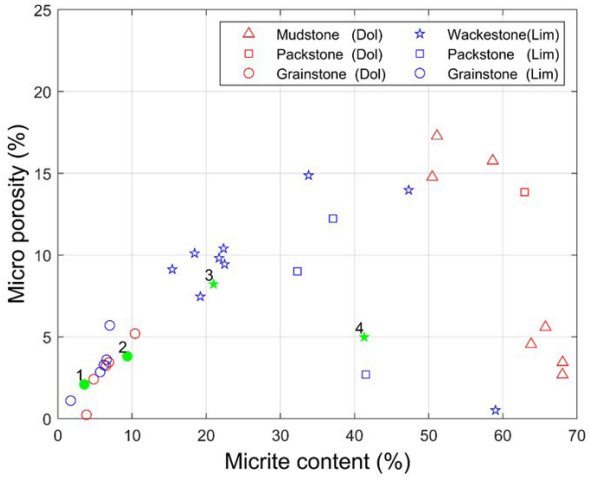

Figure 11: Shows the variation of macroporosity as a function of micrite content. Red data are the limestone samples, and blue are the dolomite samples

Figure 1 supports the conceptual model of Vanorio and Mavko (2011) that describes the evolution of the calcite grain-micrite mixture in carbonates based on grain-micrite-pore fraction and the above explanation of the variation of porosity with respect to micrite fraction (see section 1.2.3).

Micrite and Permeability Relationships

Figure 12 shows the cross-property relations between permeability and micrite content on a log-linear scale. For limestones and dolomites in Figure 12 , the micrite content ranging from 0% to 10%, the permeability shows no correlation with micrite fraction as permeability exists in all ranges. The permeability shows a peak when micrite content is around 10% and 30% and these samples were limestone wackestone. Then, permeability starts to decrease drastically for micrite content higher than 30% and the facies straddle between limestone (wackestone and packstone) and the dolomite was the only mudstone. Vanorio (2011) reported the variation of permeability with micrite did not appear to be large (permeability from 4.9 to 213.3 mD), and also noted a peak at 10% to 20% micrite content. We see a much larger dependence of permeability on micrite in our rock samples (permeability from 0.01 to 824 mD).

The numbers in black in Figure 12 refer to values measured on the samples whose microstructure is shown in Figure 1. A visual check of thin sections 1 to 4 in Figure 1 for limestone samples (dolomite samples showing similar microstructures) suggests a possible mechanism for the permeability-micrite trends seen in Figure 12.

Thin-sections 1 and 2 are grain-supported with sparry cement. For limestones and dolomites in Figure 12, permeability starts to increase with increasing micrite content approximately up to 10%. Thus, a possible mechanism for this behaviour could be due to diagenesis as sample 1 goes to sample 2 in Figure 12, the grains and sparry cement might become corroded and etched around their boundaries. The carbonate diagenesis dissolution and leaching process may transform sample 1 in Figure 1 grain stone supported to evolve toward fluid a supported rock, for example, sample 2 in Figure 1.

For limestones and dolomites in Figure 12, permeability starts to increase as micrite content deacreas from 70% up to around 30%. Thus, a possible mechanism for this behaviour could be diagenesis, as sample 4 goes to sample 3 in Figure 12, which shows that some micrite is washed out from the intergranular space. The carbonate diagenesis dissolution and leaching process leads micro-pores to become connected, with molds, large vugs and channel development leading to sample 4 in Figure 1, i.e. matrix supported evolves towards a fluid-supported rock, for example, sample 3 in Figure 1.

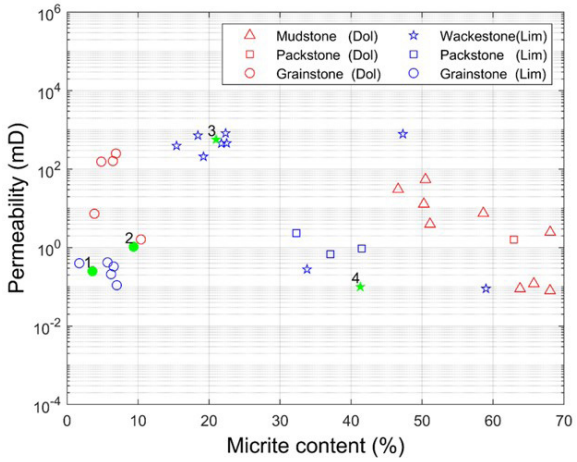

Figure 12: Shows the variation of permeability as a function of micrite content. Red data are the limestone samples, and blue are the dolomite samples

Porosity and Permeability Relationships

Figure 13 shows the cross-property relations between porosity and permeability for all 21 limestone samples and 15 dolomite samples. In general, the permeability increases as porosity increases, as expected, according

to the literature for similar rocks. (Archilha *et al.*, 2016; Costa, 2006; Dvorkin, 2009; El Husseiny & Vanorio, 2017; Fabricius *et al.*, 2010; R. Han *et al.*, 2010; Lima Neto *et al.*, 2014; Mavko & Nur, 1997; Saxena, Mavko, *et al.*, 2017; Verwer *et al.*, 2011; Vialle *et al.*, 2013; Weger *et al.*, 2009) found that Kozeny-Carmen relation fitted their observations using constant parameters B = 5, 0.5, 0.05, 0.005 overlain on Figure 13. This shows that our data are in reasonable agreement with the literature for similar oolitic limestone, sparry calcites and hydrothermal dolomites. The Kozeny-Carmen relation is

$$k=B\ (\emptyset-\emptyset_c)^2)/(1+\emptyset_c-\emptyset)^2\ d^2, \quad (9)$$

where k is permeability, B constant, d = 150 µm is diameter, $\emptyset_c$ =36 % is critical porosity and $\emptyset$ is porosity.

Also, the data points are colour-coded for micrite content and symbols for grain-supported dolomite (sparry calcite cement), matrix-supported dolomite (micrite matrix), grain-supported limestone (sparry calcite cement), matrix-supported limestone (oolitic-micrite matrix) and fluid-supported limestone (oolitic-micrite matrix with large vugs, moldic, and fenestral porosity).

Limestone samples in figure 13 shows that fluid-supported samples which was a result of diagenesis dissolution have a higher porosity-permeability than matrix-supported samples and these samples have ooids and peloids for grains. The grain-supported limestone has less than 10% micrite content and follows matrix-supported samples in porosity-permeability space. Dolomite samples show that adding micrite content seems to reduce porosity and permeability. In general, the sample with high macro porosity also has high permeability due to pore space being connected, as shown in Figure 13, with fluid-supported samples (diamond shape), and the main processing was diagenesis leaching and dissolution. However, samples with critical porosity in which the pore space is filled with micrite (matrix-supported) or sparry calcite (grain-supported limestone) in Figure 13 has implications for overall results as critical porosity samples have a high porosity but low permeability as the pore space is not connected. The critical porosity samples consider to be poor reservoir as they have lower permeability which makes the migration of hydrocarbon low.

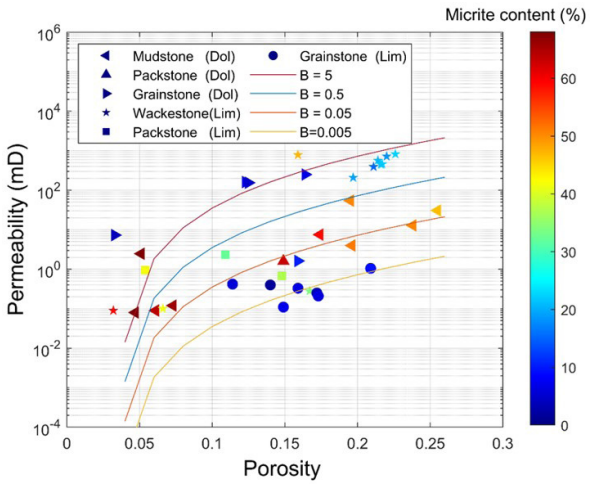

Figure 13: Shows the variation of permeability as a function of porosity. Red data are the limestone samples, and blue are the dolomite samples

El Husseiny & Vanorio (2017) investigated the effect of micrite content and macro porosity on the porosity-permeability relationships using analog samples created in a laboratory in a dual porosity system. They showed that adding micrite to grain-supported samples reduces porosity and permeability drastically, up to approximately 30% micrite content. At higher micrite contents, the sample became micrite-supported and adding more micrite only affects porosity, not permeability.

The Effect of Micrite on Elastic Wave Velocity

The variation of P-wave velocity as a function of micrite content is shown in Figure 4-15. For limestones, the velocity decrease with increasing micrite content, where a minimum in velocity is observed around 10% and 30% micrite content while the dolomites samples between 0 % and 10 % show no relationship between micrite content and velocity. Then, the velocity starts to increase with increasing micrite content above 30% (S-wave velocity shows similar).

Regarding the effect of micrite between 0 and 30% on elastic properties, we notice from a visual check of thin section 1 in Figure 1 and thin section 2 in Figure 1 that the dominant process was leaching and dissolution. The optical microscopy shows a carbonate microstructural texture mainly represented by a grain-supported framework with relatively low amounts of lime-mud interstitial material in Figure 1 and presence of tight spar cement and microcrystalline calcite forming crystal-mosaic textures and interlocked arrangements.

Figure 12 reveals that carbonate rocks characterised by micrite contents between 10% and 30% have a higher fraction of grains to micrite matrix. These carbonate samples were characterised by higher macro porosity in Figure 10, due to leaching and dispersing of microcrystalline calcite matrix that filling the grains' interstices (Vanorio & Mavko, 2011). Thus, leading to increasing of total porosity in Figure 9, and low velocity in this region.

For limestones and dolomites in Figure 15, velocity starts to decrease for micrite content lower than 10%. Thus, could be due to diagenesis as sample 1 goes to sample 2 in Figure 4.9, the grains and sparry cement might become corroded and etched around their boundaries and the facies of limestone were grain stone and wackestone. The carbonate diagenesis dissolution and leaching process may transform sample 1 grain stone supported to sample 2 fluid supported rock.

Figure 15 shows velocity to decrease with decreasing micrite content from 70% up to 30% and the dolomite were only from one facies, and it was mudstone while limestone was pack stone and wackestone. The sample is matrix supported (MS) rock microstructure predominantly constituted of aggregates of rounded, microcrystalline calcite (micrite) crystals conferring a stiff

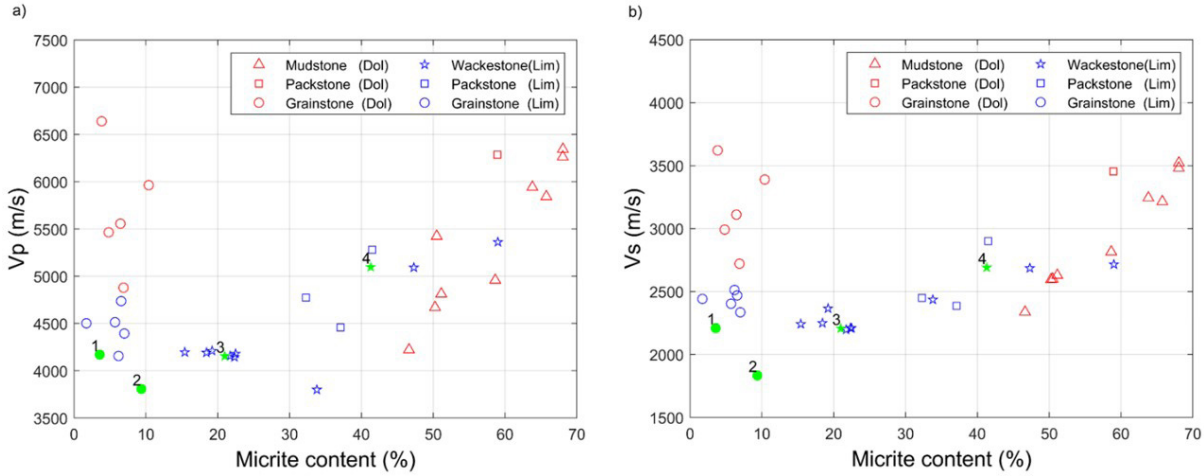

Figure 15: Shows the variation of (a) P-wave and (b) S-wave velocities as a function of micrite content

and tight texture to the rock. Hence, a significant portion of the total porosity is from small, rounded micro-pores of micrite (Vanorio & Mavko, 2011). Figure 15, Sample 3, represent fluid supported (FS).

Thin sections 3 and 4 in Figure 1 suggest some micrite was washed out from the intergranular space and this factor leads total porosity to increase. Also, the removal of micrite might reduce the effective rock stiffness as micrite (an aggregate of rounded micro-crystals) is a stiff microstructural component, therefore, both factors might reduce the velocity. Thus, the main process that leads velocity to decrease with micrite content from 70 % up to 30% is carbonate diagenesis dissolution and leaching.

Figure 16 shows the effect of pressure on velocity and micrite content. The limestone samples with micrite content of less than 10 % show very high-pressure sensitivity. Then samples between 10 and 30 % micrite content shows that the sensitivity of velocity to pressure was low. After that, the sensitivity of velocity to pressure start to slightly increase but it's less than samples with less than 10 % micrite content. The dolomite samples were very tight and was independent of pressure. Red data are the limestone samples, and blue are the dolomite samples. The numbers in black refer to values measured on the samples whose microstructure is shown in Figure 1.

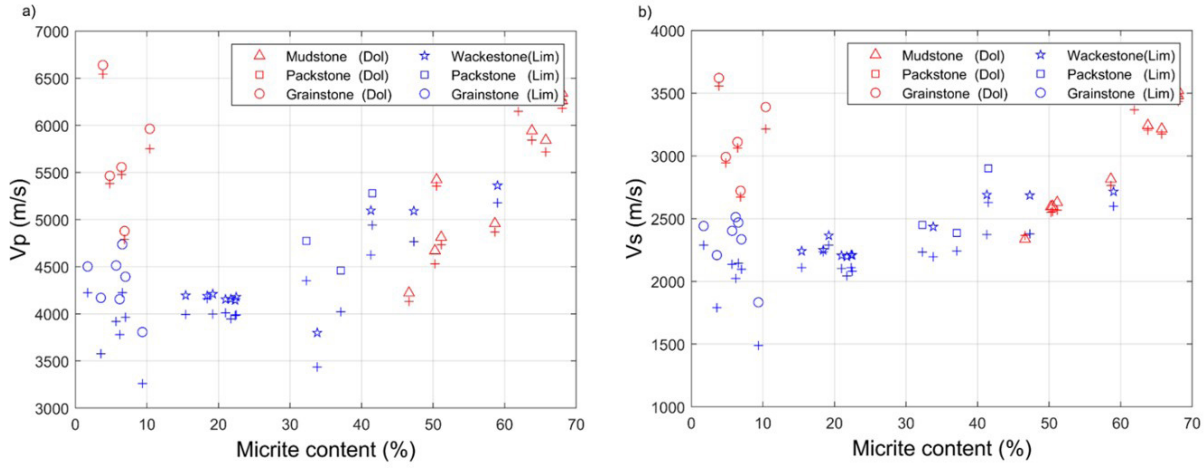

Figure 16: Pressure sensitivity of (a) P-wave and (b) S-wave velocities as function of micrite content. Data are coded as a function of pressure

This phenomenon was due to micrite-rich samples being stiffer than grain-supported samples even though micrite-rich samples had higher velocities. This suggests that the micrite-rich samples were tight, with few compliant pores, whereas grain-supported samples had more compliant pore structures. Red colour is limestone samples and blue colour is dolomite samples. The differential pressure is 50MPa and 10MPa in plus sign.

These results agree with (Husseiny & Vanorio, 2015), for the relation between velocity and micrite content as they made a synthetic carbonate rock of two sets of data, one without cement and the other sets of data with cement. Husseiny & Vanorio *et al.*, (2015) show that micrite-rich samples characterised by larger acoustic velocities for both the uncemented and cemented samples which suggests that the presence of cement was not the main controlling

factor. Husseiny & Vanorio *et al.*, (2015) explained this phenomenon by velocity sensitivity to pressure as the sensitivity of velocity to pressure increases as the micrite content decreases. In the contrary, while the sensitivity of velocity to pressure increases, the micrite content decreases which indicate that grain-supported samples have a more compliant structure.

The Effect of Micrite on Attenuation

Seismic attenuation is a great attribute that can be utilised as an indicator of fracture, lithology, clay, fluid content and pore structure in a reservoir rock (Parra, 2006). The cross-property relations between micrite content and Qp-1 and Qs-1 are shown in Figure 14 (a, b), respectively. The data shows a non-linear relationship. Also, it is sparse and scattered. However, the quality factors show two peaks: the first peak was around 10% micrite content and, the dominant facies were grainstone, and the second peak was around 40% micrite content. The facies were straddled between mudstone, packstone and wackstone, forming a bell-shaped correlation between Qp-1 and micrite (Qs-1 show similar results).

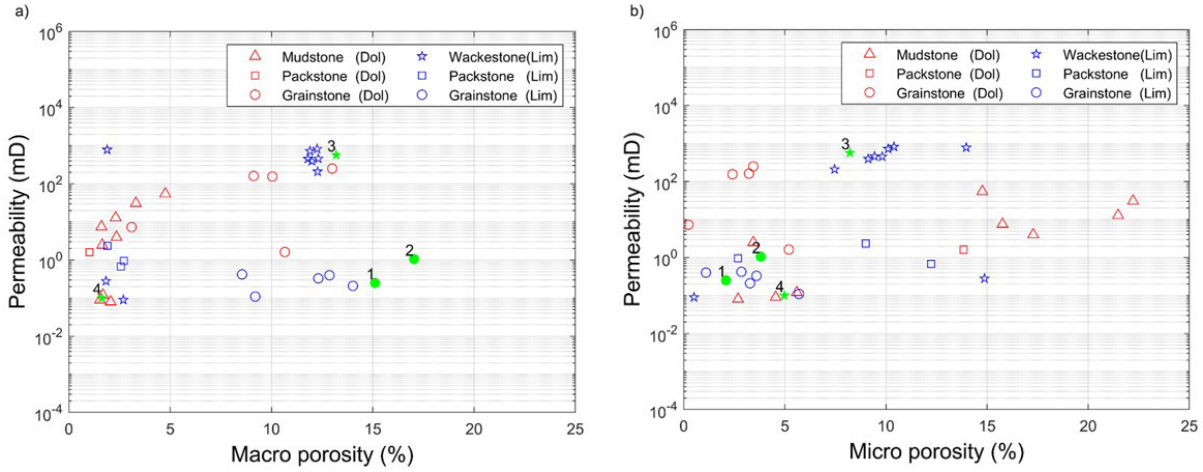

Figure 14: Shows the variation of permeability as a function of a) microporosity b) macroporosity. Red data are the limestone samples, and blue are the dolomite samples

Figure 17 shows the sensitivity of the attenuation to pressure as a function of micrite content. We notice that the two peaks were more pressure sensitive, which indicates the closure of cracks and microcracks in these samples from 10 MPa to 50 MPa. The possible mechanism to explain the attenuation behaviour with respect to micrite was Biot mechanism (Global fluid flow). Further, in the two peaks, the closure of cracks and the microcracks were very high as shown in Figure 18 so another mechanism is possible here and it is the Squirt-flow mechanism. The squirt-flow mechanism focuses on the loss resulting from the 'local' flow of viscous fluid into and out of microcracks during the passage of acoustic waves. Assefa, McCann and Sothcott, (1999) studied the effect of attenuation on facies such as mudstone, wackestone, grainstone and packstone. They concluded that when the attenuation reaches the maximum values, the dual porosity system is developed, indicating that the squirt-flow mechanism, which has previously been shown to occur in shaley sandstones, also operates in the limestones.

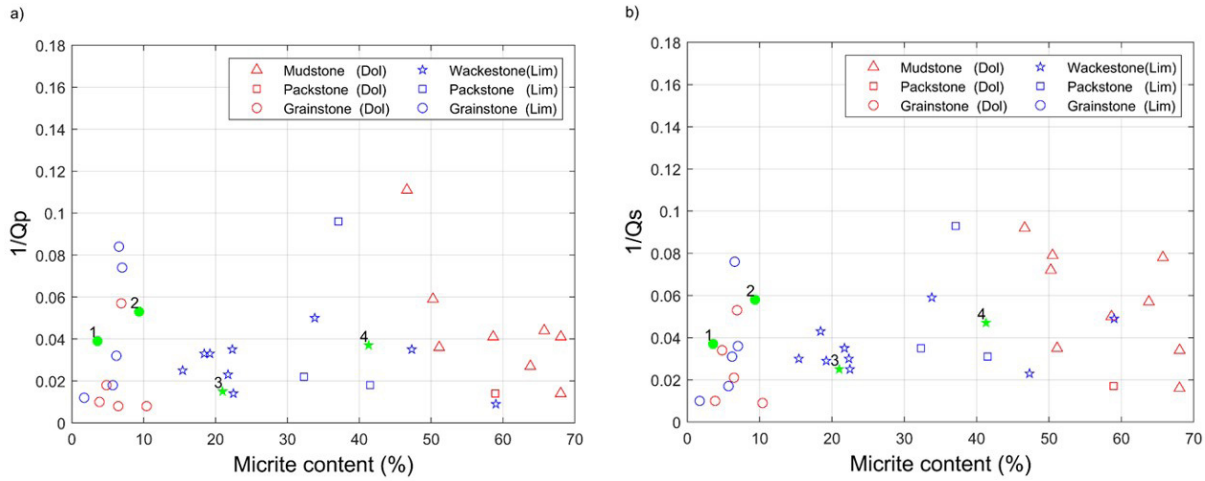

Figure 17: Shows the variation of a) P-wave b) S-wave quality factors as a function of micrite content. Red data are the limestone samples, and blue are the dolomite samples

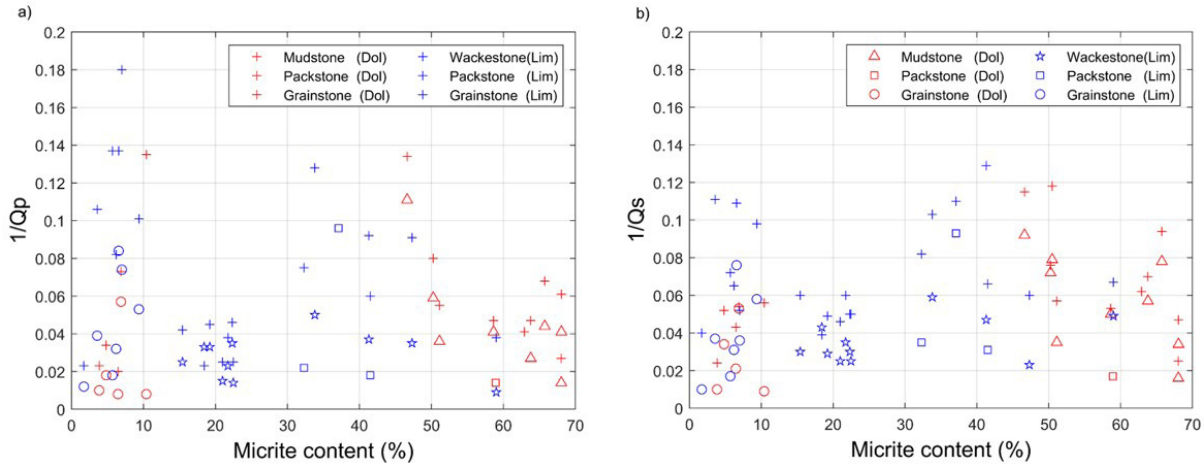

Figure 18: Shows the pressure sensitivity of a) P-wave b) S-wave quality factors as a function of micrite content. Red data are the limestone samples, and blue are the dolomite samples. The differential pressure is 50MPa and 10MPa in plus sign

The Effect of Micrite on Electrical Resistivity

Electrical resistivity is affected by key characteristic which is pore structure as the connectivity and size of the pores control the overall pore network connection, and the pore throats will be affected by capillary forces. Many controlling factors affect Electrical resistivity such as (1) size of the pore throats (Abousrafa *et al.*, 2009), (2) on the amount of separate-vugs porosity (Lucia & Conti, 1987), and (3) tortuosity (Saner *et al.*, 1996).

Apparent electrical formation factor F* (defined as ϱ_0/ϱ_w, where ϱ_w =0.213 Ωm for 35 g/l brine at a temperature of 19°C) measured at 80 Hz versus microcrystalline calcite for all 21 samples of limestone and 15 samples dolomite are shown in Figure 19 on a log-linear scale. Apparent formation factor F* shows, in general, a U-shape trend with a general decreasing trend with increasing microcrystalline calcite for samples below 15% microcrystalline calcite margin. Apparent electrical formation factor F* at the lowest value between 10 and 30 % microcrystalline calcite. Figure 19 shows an increasing trend of apparent formation factor F* with microcrystalline calcite for the limestone samples above 30% microcrystalline calcite, and a steep decrease in F* with micrite for dolomites. These data show the opposite trend to the permeability data in Fig 4.12, as would be expected, as F* is an analogous transport property.

Figure 19 shows apparent formation factors against micrite content. The apparent formation factors start to decrease when the micrite content below 10%. A visual check of the thin sections 1 and 2 in figure 19, corresponds to sample number 1 and 2 in Figure 1, grain stone and fluid supported respectively.

Thus, could be due to diagenesis as, sample 1 goes to sample 2 in Figure 1, the grains and sparry cement might become corroded and etched around their boundaries. The carbonate diagenesis dissolution and leaching process may transform sample 1 grain stone supported to sample 2 fluid supported rock. This will lead porosity to increase as shown in Figure 9 and the macro porosity will be connected and form secondary porosity such as, vugs, moldic and fenestral as shown in Figure 10.

The apparent formation factors have the lowest value between micrite content 20-30 % due to the presence of both, macro porosity (vugs) and micro porosity within micrite content so the conductivity is high. Figure 19 shows the apparent formation factors increase as micrite content increase above 30% micrite content with two trends parallel to each other and oolitic limestone samples higher than dolomite samples.

A visual check of the thin sections 3 and 4 in Figure 1, corresponds to sample 3 and 4 in Figure 19, which both are oolitic limestone (wackestone) as shown in red colour in Figure 19. Sample 3, represent fluid supported (FS) and sample 4 represent matrix supported (MS). The red colour samples above 30% micrite in Figure 19 shows first trend and these samples are limestone characterised by large grains (oolite) and fine grains (micrite). The blue colour samples above 30% micrite in Figure 19 are dolomite samples with majority of rocks are fine grains (micrite) and they are matrix supported (MS) rock microstructure predominantly constituted of aggregates of rounded, microcrystalline calcite (micrite) crystals conferring a stiff and tight texture to the rock (Figure 7 A). Hence, a significant portion of the total porosity were from small, rounded micropores of micrite (Vanorio & Mavko, 2011).

For limestones and dolomites in Figure 19, the carbonate samples above 30% micrite have higher apparent formation factors as micrite seems to reduce the mean pore size and the overall porosity and block the electrolyte conduction due to a reduction in connectivity between the pores.

The apparent formation factors start to decrease as micrite content decreases from 70% up to around 30 %. The thin sections 3 and 4 in Figure 1 suggest a possible mechanism for this behaviour, and it could be due to

diagenesis as, sample 4 goes to sample 3 in Figure 19, which shows that some of micrite is washed out from the intergranular space.

The carbonate diagenesis dissolution and leaching process lead micropores to become connected, molds, large vugs, and channel might develop, leading sample 4 in Figure 1 matrix supported to evolve toward fluid-supported rock, for example, sample 3 in Figure 1. The apparent formation factor data show the opposite trend to the permeability data in Fig 12, and porosity data in Fig 9 as would be expected, as F* is an analogous transport property. Thus, the main factor that affect F* in carbonate rocks seems to be the porosity and micrite content, due to porosity and micrite content were highly negatively correlated for the majority of our samples. The main process that leads apparent formation factors to decreases with micrite content from 70 % up to 30% is carbonate diagenesis dissolution and leaching.

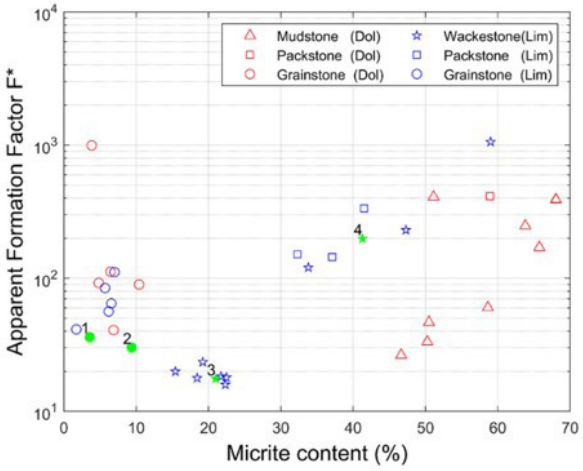

Figure 19: Shows the variation of apparent formation factors as a function of micrite content. Red data are the limestone samples, and blue are the dolomite samples

The matrix-supported samples having most of the porosity in the type of microporosity and the grain-supported samples having the most of the porosity as microporous and vugs, might suggest that microporosity, pore network connectivity, pore size of macro porosity might a have a significant influence in F* rather than pore size. Verwer *et al.* (2011) suggest that for carbonate rocks, the significant controlling factor for resistivity were both pore structure and the absolute number of pores, regardless of the size of the pore throats based on seventy-one plugs from boreholes and digital image analysis.

CONCLUSION

The study presented a methodological approach to estimate microstructural parameters such as micrite content and macro porosity in a carbonate rock based on image analysis obtained from the optical microscope. The image analysis technique was an effective, accurate, and easy method of measuring Micrite aggregate and macro porosity. The study also quantified the uncertainty associated with the estimated parameters by using standard deviation. The amount of micrite aggregate obtained was compared by two techniques: the point counting method and image analysis using ImageJ software. The error seems to be larger when micrite aggregate is around (30% - 50%). The research findings suggested that Carbonate samples with higher micrite content and lower macroporosity have lower permeability at any given porosity. Moreover, the study also quantified the uncertainty associated with the estimated parameters and found that optical microscope images can reproduce microstructural parameters with an average root mean square error of 6%.

REFERENCES

Abousrafa, E. M., Somerville, J. M., Hamilton, S. A., Olden, P. W. H., Smart, B. D. G., & Ford, J. (2009). Pore geometrical model for the resistivity of brine saturated rocks. *Journal of Petroleum Science and Engineering, 65*(3–4), 113–122. https://doi.org/10.1016/j.petrol.2008.12.009

Adams, A E, Guilford, C., & MacKenzie, W. S. (1984). Atlas of sedimentary rocks under the microscope.

Adams, Anthony E, MacKenzie, W. S., & Guilford, C. (2017). Atlas of sedimentary rocks under the microscope. Routledge.

Archilha, N. L., Missagia, R. M., Hollis, C., De Ceia, M. A. R., McDonald, S. A., Lima Neto, I. A., Eastwood, D. S., & Lee, P. (2016). Permeability and acoustic velocity controlling factors determined from x-ray tomography images of carbonate rocks. *AAPG Bulletin, 100*(8), 1289–1309. https://doi.org/10.1306/02251615044

Assefa, S., McCann, C., & Sothcott, J. (1999). Attenuation of P- and S-waves in limestones. *Geophysical Prospecting, 47*(3), 359–392. https://doi.org/10.1046/j.1365-2478.1999.00136.x

Baechle, G. T., Weger, R. J., Eberli, G. P., & Massaferro, J. L. (2004). The role of macroporosity and microporosity in constraining uncertainties and in relating velocity to permeability in carbonate rocks. 74th Ann. *Internat. Mtg., January 2004,* 1662–1665. https://doi.org/10.1190/1.1845149

Berhanu, S. A. (1994a). Seismic and Petrophysical Properties of Carbonate.

Berhanu, S. A. (1994b). SEISMIC AND PETROPHYSICAL PROPERTIES OF CARBONATE.

Brigaud, B., Vincent, B., Durlet, C., Deconinck, J.-F., Blanc, P., & Trouiller, A. (2010). Acoustic Properties of Ancient Shallow-Marine Carbonates: Effects of Depositional Environments and Diagenetic Processes (Middle Jurassic, Paris Basin, France). *Journal of Sedimentary Research, 80*(9), 791–807. https://doi.org/10.2110/jsr.2010.071

Cantrell, D. L., & Hagerty, R. M. (1999). Microporosity in Arab Formation Carbonates, Saudi Arabia. *GeoArabia, 4*(2), 129–154.

Ceia, M., Neto, I. L., Missagia, R., Oliveira, G., Santos, V., Paranhos, R., & Archilha, N. (2017). Evaluation of microporosity aspect ratio and shear wave velocity of middle-east carbonates. 3755–3759.

Chilingar, G. V, Bissell, H. J., & Fairbridge, R. W. (1967). Carbonate rocks. Elsevier.

Costa, A. (2006). Permeability-porosity relationship: A reexamination of the Kozeny-Carman equation based on a fractal pore-space geometry assumption. *Geophysical Research Letters, 33*(2), 1–5. https://doi.org/10.1029/2005GL025134

Croizé, D., Ehrenberg, S. N., Bjørlykke, K., Renard, F., & Jahren, J. (2010). Petrophysical properties of bioclastic platform carbonates: Implications for porosity controls during burial. *Marine and Petroleum Geology, 27*(8), 1765–1774. https://doi.org/10.1016/j.marpetgeo.2009.11.008

Dunham, R. J. (1962). Classification of carbonate rocks according to depositional textures.

Dvorkin, J. (2009). Kozeny-Carman equation revisited. Pangea.Stanford.Edu/~jack/KC_2009_JD.Pdf, 1–16.

Eberli, G. P., Baechle, G. T., Anselmetti, F. S., & Incze, M. L. (2003). Factors controlling elastic properties in carbonate sediments and rocks. *The Leading Edge, 22*(7), 654–660. https://doi.org/10.1190/1.1599691

El Husseiny, A., & Vanorio, T. (2017). Porosity-permeability relationship in dual-porosity carbonate analogs. *Geophysics, 82*(1), MR65–MR74. https://doi.org/10.1190/geo2015-0649.1

Fabricius, I. L., Bächle, G. T., & Eberli, G. P. (2010). Elastic moduli of dry and water-saturated carbonates — Effect of depositional texture, porosity, and permeability. *Geophysics, 75*(3), N65–N78. https://doi.org/10.1190/1.3374690

Folk, R. L. (1959). Practical petrographic classification of limestones. *AAPG Bulletin, 43*(1), 1–38.

Fournier, F., & Borgomano, J. (2009). Critical porosity and elastic properties of microporous mixed carbonate-siliciclastic rocks. *Geophysics, 74*(2), E93–E109. https://doi.org/10.1190/1.3043727

Grasby, S. E., & Betcher, R. N. (2002). Regional hydrogeochemistry of the carbonate rock aquifer, southern Manitoba. *Canadian Journal of Earth Sciences, 39*(7), 1053–1063.

Grove, C., & Jerram, D. A. (2011). JPOR: An ImageJ macro to quantify total optical porosity from blue-stained thin sections. *Computers and Geosciences, 37*(11), 1850–1859. https://doi.org/10.1016/j.cageo.2011.03.002

Haines, T. J., Neilson, J. E., Healy, D., Michie, E. A. H., & Aplin, A. C. (2015). The impact of carbonate texture on the quantification of total porosity by image analysis. *Computers and Geosciences, 85,* 112–125. https://doi.org/10.1016/j.cageo.2015.08.016

Hamilton, C. W. (2010). Computers & Geosciences New image processing software for analysing object size-frequency distributions , geometry , orientation , and spatial distribution $. 36, 539–549. https://doi.org/10.1016/j.cageo.2009.09.003

Han, D. (1986). Effects of porosity and clay content on wave velocities in sandstones. *Geophysics, 51*(11), 2093. https://doi.org/10.1190/1.1442062

Han, R., Hirose, T., & Shimamoto, T. (2010). Strong velocity weakening and powder lubrication of simulated carbonate faults at seismic slip rates. *Journal of Geophysical Research: Solid Earth, 115*(3). https://doi.org/10.1029/2008JB006136

Hawkins, P., Tennis, P. D., & Detwiler, R. J. (1996). The use of limestone in Portland cement: a state-of-the-art review. Portland Cement Association.

Higgins, Michael D, & Roberge, J. (2007). Three magmatic components in the 1973 eruption of Eldfell volcano, Iceland: Evidence from plagioclase crystal size distribution (CSD) and geochemistry. *Journal of Volcanology and Geothermal Research, 161*(3), 247–260.

Higgins, Michael Denis. (2006). Quantitative textural measurements in igneous and metamorphic petrology. Cambridge University Press.

Husseiny, A. El, & Vanorio, T. (2015). The effect of micrite content on the acoustic velocity of carbonate rocks. 80(4). https://doi.org/10.1190/geo2014-0599.1

Jerram, D A, & Higgins, M. D. (2007). 3D analysis of rock textures: Quantifying igneous microstructures: Elements, v. 3. https://doi.org/10, 239–245.

Jerram, Dougal A, Mock, A., Davis, G. R., Field, M., & Brown, R. J. (2009). Lithos 3D crystal size distributions : A case study on quantifying olivine populations in kimberlites. *LITHOS, 112,* 223–235. https://doi.org/10.1016/j.lithos.2009.05.042

Kazatchenko, E., Markov, M., Mousatov, A., & Parra, J. (2006). Carbonate microstructure determination by inversion of acoustic and electrical data: Application to a south Florida aquifer. *Journal of Applied Geophysics, 59*(1), 1–15. https://doi.org/10.1016/j.jappgeo.2005.07.004

Kowallis, B. J., Jones, L. E. a., & Wang, H. F. (1984). Velocity-porosity-clay content systematics of poorly consolidated sandstones. *Journal of Geophysical Research, 89,* 10355. https://doi.org/10.1029/JB089iB12p10355

Lambert, L., Durlet, C., Loreau, J. P., & Marnier, G. (2006). Burial dissolution of micrite in Middle East carbonate reservoirs (Jurassic-Cretaceous): Keys for recognition and timing. *Marine and Petroleum Geology, 23*(1), 79–92. https://doi.org/10.1016/j.marpetgeo.2005.04.003

Lima Neto, I. A., Misságia, R. M., Ceia, M. A., Archilha, N. L., & Oliveira, L. C. (2014). Carbonate pore system evaluation using the velocity-porosity-pressure relationship, digital image analysis, and differential effective medium theory. *Journal of Applied Geophysics, 110,* 23–33. https://doi.org/10.1016/j.jappgeo.2014.08.013

Lucia, F. J., & Conti, R. D. (1987). Rock fabric, permeability, and log relationships in an upward-shoaling, vuggy

carbonate sequence.
Mackenzie, W. S/ Guilford, C. (1980). Atlas of rocks-Forming minerals in thin section. 93.
Mackenzie, W. S., Guilford, C., & Scientific, L. (1980). Atlas of rock-forming minerals in thin sections.
Marion, D., Nur, A., Yin, H., & Han, D. H. (1992). Compressional velocity and porosity in sand-clay mixtures. *Geophysics, 57*(4), 554-563. https://doi.org/10.1190/1.1443269
Marion, Dominique. (1990). Acoustical, Mechanical, And Transport Properties Of Sediments And Granular Materials. *Geophysics, 39,* 136.
Marks, S. G. (1994). Seismic wave attenuation from vertical seismic profiles. University of Reading.
Mavko, G., & Nur, A. (1997). Short Note The effect of a percolation threshold in the Kozeny-Carman relation Gary Mavko * and Amos Nur *. *Most, 62*(5), 1480–1482.
Norbisrath, J. H., Eberli, G. P., Laurich, B., Desbois, G., Weger, R. J., & Urai, J. L. (2015). Electrical and fluid flow properties of carbonate microporosity types from multiscale digital image analysis and mercury injection. *AAPG Bulletin, 99*(11), 2077–2098. https://doi.org/10.1306/07061514205
(North *et al.*, 2013), Laurence, Best, A. I., Sothcott, J., & Macgregor, L. (2013). Laboratory determination of the full electrical resistivity tensor of heterogeneous carbonate rocks at elevated pressures. *Geophysical Prospecting, 61*(2), 458–470. https://doi.org/10.1111/j.1365-2478.2012.01113.x
(North *et al.*, 2013), LJ, Best, A., & Sothcott, J. (2012). Pressure Sensitivity of the Joint Elastic-electrical Properties of Carbonate Reservoir Rocks. 74th EAGE Conference & Exhibition, June 2012, 4–7. http://www.earthdoc.org/publication/publicationdetails/?publication=59270
Parra, J. O., & Hackert, C. L. (2006). Modeling and interpretation of Q logs in carbonate rock using a double porosity model and well logs. *Journal of Applied Geophysics, 58*(3), 253–262. https://doi.org/10.1016/j.jappgeo.2005.07.003
Rasband, W. S. (1997). ImageJ. US National Institutes of Health, Bethesda, MD.
Regnet, J. B., Robion, P., David, C., Fortin, J., Brigaud, B., & Yven, B. (2015). Acoustic and reservoir properties of microporous carbonate rocks: Implication of micrite particle size and morphology. *Journal of Geophysical Research: Solid Earth, 120*(2), 790–811. https://doi.org/10.1002/2014JB011313
Saner, S., Al-Harthi, A., & Htay, M. T. (1996). Use of tortuosity for discriminating electro-facies to interpret the electrical parameters of carbonate reservoir rocks. *Journal of Petroleum Science and Engineering, 16*(4), 237–249. https://doi.org/10.1016/S0920-4105(96)00045-9
Saxena, N., Hofmann, R., Alpak, F. O., Dietderich, J., Hunter, S., & Day-Stirrat, R. J. (2017). Effect of image segmentation & voxel size on micro-CT computed effective transport & elastic properties. *Marine and Petroleum Geology, 86,* 972–990. https://doi.org/10.1016/j.marpetgeo.2017.07.004
Saxena, N., Mavko, G., Hofmann, R., & Srisutthiyakorn, N. (2017). Estimating permeability from thin sections without reconstruction: Digital rock study of 3D properties from 2D images. *Computers and Geosciences, 102*(February), 79–99. https://doi.org/10.1016/j.cageo.2017.02.014
Sellwood, B. W., Shepherd, T. J., Evans, M. R., & James, B. (1989). Origin of late cements in oolitic reservoir facies: a fluid inclusion and isotopic study (Mid-Jurassic, southern England). *Sedimentary Geology, 61*(3–4), 223–237. https://doi.org/10.1016/0037-0738(89)90059-6
Vanorio, T., & Mavko, G. (2011). Laboratory measurements of the acoustic and transport properties of carbonate rocks and their link with the amount of microcrystalline matrix. *Geophysics, 76*(4), E105–E115. https://doi.org/10.1190/1.3580632
Verwer, K., Eberli, G. P., & Weger, R. J. (2011). Effect of pore structure on electrical resistivity in carbonates. *AAPG Bulletin, 95*(2), 175–190. https://doi.org/10.1306/06301010047
Vialle, S., Dvorkin, J., & Mavko, G. (2013). Implications of pore microgeometry heterogeneity for the movement and chemical reactivity of in carbonates. *Geophysics, 78*(5), L69–L86. https://doi.org/10.1190/geo2012-0458.1
Weger, R. J., Eberli, G. P., Baechle, G. T., Massaferro, J. L., & Sun, Y. F. (2009). Quantification of pore structure and its effect on sonic velocity and permeability in carbonates. *AAPG Bulletin, 93*(10), 1297–1317. https://doi.org/10.1306/05270909001

APPENDIX I

Petrophysical and Facies properties of the 36 carbonate samples

Sample ID	Measured physical properties		Microstructural parameters estimated from optical microscopy images				Facies
Limestone	Porosity (%)	Permeability (mD)	Φ macro (%)	Φ micro (%)	f grains	f micrite	Facies
Base Bed 2	21.747	458.000	12.310	9.437	55.773	22.480	WKST
Base Bed 3	21.410	569.000	13.190	8.220	57.600	20.990	WKST
Base Bed 4	22.646	824.000	12.250	10.396	55.024	22.330	WKST
BWB 2	21.615	452.000	11.800	9.815	56.655	21.730	WKST

BWB 3	21.111	393.000	11.990	9.121	63.469	15.420	WKST
BWB 4	22.004	723.000	11.900	10.104	59.566	18.430	WKST
Pond Free Stone	13.962	0.400	12.862	1.100	84.318	1.720	GRST
RS08A	17.200	0.250	15.110	2.090	79.230	3.570	GRST
RS08B	20.850	1.050	17.040	3.810	69.780	9.370	GRST
RS08C	15.910	0.330	12.310	3.600	77.530	6.560	GRST
WB 2	19.736	209.000	12.276	7.460	61.054	19.210	WKST
S-39400	3.200	0.090	2.690	0.510	37.800	59.000	WKST
S-39415	16.700	0.280	1.830	14.870	49.500	33.800	WKST
S-39433	5.400	0.950	2.710	2.690	53.100	41.500	PKST
S-39437	14.900	0.110	9.200	5.700	78.100	7.000	GRST
S-39438	17.300	0.210	14.020	3.280	76.500	6.200	GRST
S-39440	11.400	0.420	8.550	2.850	82.900	5.700	GRST
S-39446	6.600	0.100	1.620	4.980	52.100	41.300	WKST
S-39448	14.800	0.680	2.570	12.230	48.100	37.100	PKST
S-39454	15.860	785.000	1.890	13.970	36.840	47.300	WKST
S-39464	10.900	2.340	1.900	9.000	56.800	32.300	PKST

Sample ID	**Measured physical properties**		**Microstructural parameters estimated from optical microscopy images**				
Dolomite	**Porosity (%)**	**Permeability (mD)**	**Φ macro (%)**	**Φ micro (%)**	**f grains**	**f micrite**	**Facies**
Alg 1.1	23.788	12.860	2.310	21.478	25.962	50.250	MST
Alg 1.3	25.527	30.700	3.310	22.217	27.843	46.630	MST
Bio 1.1	19.631	3.980	2.350	17.281	29.249	51.120	MST
Bio 2.2	19.524	54.660	4.760	14.764	29.996	50.480	MST
BM 1	6.088	0.090	1.540	4.548	30.112	63.800	MST
BM 2	7.273	0.120	1.680	5.593	26.987	65.740	MST
BM 3	4.747	0.080	2.060	2.687	27.223	68.030	MST
BM 4	5.092	2.470	1.650	3.442	26.858	68.050	MST
BV 2	17.373	7.500	1.610	15.763	23.997	58.630	MST
GRN 1	3.332	7.300	3.100	0.232	92.818	3.850	GRST
GRN 2	12.349	161.000	9.119	3.230	81.191	6.460	GRST
GRN 3	12.454	155.000	10.044	2.410	82.726	4.820	GRST
GRN 4	16.440	250.200	13.000	3.440	76.680	6.880	GRST
S-39456	15.860	1.620	10.660	5.200	73.740	10.400	GRST
S-39457	14.860	1.600	1.020	13.840	26.230	58.910	PKST

APPENDIX II: Joint Elastic-Electrical Measurement Results on the 36 Carbonate Samples Studied in This Paper

Sample	**60 MPa**						**50 MPa**					
	Vp	**Qp**	**Vs**	**Qs**	**ϱ**	**F**	**Vp**	**Qp**	**Vs**	**Qs**	**ϱ**	**F**
Base Bed 2	4184	61.768	2214	43.873	3.861	18.125	4179	70.054	2209	39.958	3.824	17.954
Base Bed 3	4164	64.231	2217	49.244	3.841	18.034	4154	67.322	2206	39.834	3.742	17.567
Base Bed 4	4149	27.303	2218	36.277	3.399	15.957	4144	28.257	2210	33.282	3.383	15.882

BWB 2	4164	42.715	2202	29.015	3.919	18.398	4156	42.733	2197	28.806	3.895	18.287			
BWB 3	4206	38.299	2246	31.156	4.275	20.071	4195	39.666	2241	32.922	4.247	19.937			
BWB 4	4192	28.605	2250	26.319	3.838	18.020	4191	29.854	2249	23.329	3.788	17.784			
Pond Free Stone	4526	78.047	2454	114.892	8.860	41.598	4502	83.982	2441	102.666	8.812	41.372			
RS08A	4218	27.895	2234	30.072	7.791	36.579	4170	25.869	2209	26.955	7.698	36.141			
RS08B	3859	19.626	1873	17.326	6.484	30.439	3807	18.939	1833	17.357	6.430	30.189			
RS08C	4786	12.405	2508	13.995	13.932	65.408	4737	11.874	2469	13.168	13.789	64.737			
WB 2	4236	29.512	2369	36.909	5.031	23.618	4210	30.422	2365	34.716	5.001	23.479			
S-39400							5361	117.090	2715	20.365	225.221	1057.376			
S-39415							3799	20.137	2435	17.090	25.638	120.365			
S-39433							5279	54.459	2900	32.400	71.296	334.723			
S-39437							4394	13.447	2335	27.973	23.675	111.150			
S-39438							4156	30.836	2512	32.208	11.998	56.326			
S-39440							4513	54.288	2403	58.392	18.003	84.521			
S-39446							5096	27.010	2690	21.182	42.204	198.141			
S-39448							4459	10.411	2386	10.702	30.685	144.063			
S-39454							5091	28.787	2685	43.736	49.068	230.368			
S-39464							4773	45.612	2449	28.516	32.301	151.646			

Alg 1.1	4686	16.832	2615	16.171	7.275	34.155	4670	16.952	2595	13.977	7.095	33.312						
Alg 1.3	4233	8.984	2378	10.847	5.788	27.172	4222	8.989	2337	10.922	5.641	26.486						
Bio 1.1	4828	29.351	2635	32.053	91.564	429.879	4813	27.946	2629	28.289	86.915	408.051						
Bio 2.2	5438	6.122	2592	13.437	10.111	47.471	5423	5.917	2598	12.716	9.953	46.726						
BM 1	5955	38.369	3258	24.206	54.318	255.014	5942	37.074	3243	17.562	52.723	247.526						
BM 2	5858	22.744	3216	12.406	38.292	179.774	5842	22.905	3214	12.864	36.361	170.710						
BM 3	6284	67.313	3499	164.731	85.963	403.582	6262	72.254	3480	64.458	83.174	390.488						
BM 4	6358	23.927	3535	32.642	85.811	402.869	6343	24.534	3521	29.626	82.745	388.474						
BV 2	4969	23.276	2824	19.122	13.319	62.532	4958	24.566	2815	19.920	12.820	60.188						
GRN 1	6659	96.499	3629	100.429	231.770	1088.122	6639	100.557	3620	95.841	211.940	995.023						
GRN 2	5566	111.912	3118	46.662	24.506	115.052	5556	118.540	3110	46.786	23.867	112.052						
GRN 3	5478	54.473	2999	30.208	19.940	93.615	5464	56.886	2991	29.670	19.687	92.427						
GRN 4	4901	18.529	2726	16.989	8.827	41.442	4878	17.567	2721	18.999	8.690	40.796						
S-39456							5963	123.534	3389	108.926	19.105	89.692						
S-39457							6285	73.051	3453	59.061	88.146	413.831						
Sample	**40 MPa**						**30 MPa**											
	Vp	**Qp**	**Vs**	**Qs**	**ϱ**	**F**	**Vp**	**Qp**	**Vs**	**Qs**	**ϱ**	**F**						
Base Bed 2	4157	72.156	2194	37.582	3.786	17.775	4123	68.274	2174	34.090	0.000	0.000						
Base Bed 3	4134	67.419	2195	47.677	3.687	17.310	4103	62.931	2174	32.577	3.674	17.249						
Base Bed 4	4123	28.553	2200	33.059	3.374	15.841	4093	28.255	2181	27.440	3.368	15.811						

BWB 2	4128	40.087		2177	27.849		3.866		18.149	4094	38.697		2156		24.393		3.835		18.005	
BWB 3	4177	40.368		2231	30.361		4.206		19.745	4139	36.428		2205		28.087		4.178		19.615	
BWB 4	4185	31.851		2242	25.997		3.742		17.568	4182	35.795		2247		29.308		3.718		17.454	
Pond Free Stone	4477	91.872		2426	89.946		8.771		41.178	4428	89.089		2402		71.426		8.718		40.931	
RS08A	4080	22.229		2149	19.207		7.466		35.051	3950	19.254		2042		16.108		7.592		35.642	
RS08B	3734	17.231		1775	14.929		6.406		30.077	3626	15.122		1717		10.060		6.465		30.353	
RS08C	4656	10.862		2431	12.577		13.693		64.286	4546	9.619		2381		9.840		13.525		63.498	
WB 2	4179	29.175		2352	32.162		4.975		23.355	4138	28.352		2340		29.991		4.948		23.230	
S-39400	5336	103.271		2709	17.490		243.596		1143.643	5297	71.927		2694		16.106		278.896		1309.371	
S-39415	3765	17.357		2412	16.028		24.183		113.537	3708	14.196		2377		12.602		25.407		119.281	
S-39433	5247	48.876		2856	24.079		53.639		251.828	5196	38.917		2758		20.337		63.516		298.195	
S-39437	4342	12.319		2321	22.631		23.777		111.629	4247	10.419		2279		22.169		22.065		103.590	
S-39438	4114	28.766		2479	18.672		11.905		55.891	4050	22.725		2367		17.398		12.045		56.550	
S-39440	4482	46.432		2391	54.739		17.813		83.627	4422	32.896		2346		41.762		17.790		83.522	
S-39446	5060	26.435		2648	18.932		42.046		197.400	4988	22.559		2584		15.847		41.799		196.238	
S-39448	4409	10.094		2372	9.806		31.273		146.822	4331	9.173		2345		9.546		30.888		145.015	
S-39454	5064	27.504		2675	40.702		49.757		233.599	5014	23.749		2625		28.690		50.067		235.057	
S-39464	4736	41.451		2421	19.384		32.525		152.700	4669	32.649		2353		17.042		30.957		145.338	
Alg 1.1	4638	17.070		2575	13.780		6.816		31.998	4597	17.228		2560		15.513		6.569		30.841	

Alg 1.3	4203	8.674	2319	11.489	5.332	25.032	4168	8.208	2333	11.708	5.258	24.686
Bio 1.1	4806	36.400	2615	25.988	81.573	382.972	4790	31.000	2601	25.709	73.073	343.068
Bio 2.2	5408	5.805	2589	9.815	9.678	45.438	5360	5.372	2552	12.099	8.974	42.130
BM 1	5916	34.993	3206	18.502	51.165	240.211	5887	31.220	3205	20.227	49.556	232.657
BM 2	5813	23.005	3195	14.334	34.971	164.181	5768	21.996	3188	11.900	33.859	158.963
BM 3	6239	65.464	3459	74.956	79.876	375.005	6214	54.309	3455	84.384	75.830	356.009
BM 4	6319	23.933	3511	29.665	79.626	373.831	6293	21.113	3496	25.937	74.946	351.859
BV 2	4938	25.137	2809	17.155	12.784	60.017	4919	25.254	2775	17.803	11.728	55.062
GRN 1	6613	86.026	3606	79.180	194.140	911.455	6582	69.144	3581	72.344	174.930	821.268
GRN 2	5537	115.107	3104	43.331	23.590	110.751	5511	101.028	3087	35.799	22.794	107.014
GRN 3	5449	51.769	2981	28.555	19.187	90.080	5424	48.953	2969	27.762	17.238	80.930
GRN 4	4857	16.934	2707	18.364	8.611	40.425	4834	16.243	2690	18.641	8.523	40.014
S-39456	5924	73.873	3352	66.237	20.454	96.028	5862	41.390	3295	41.688	17.805	83.590
S-39457	6261	69.957	3429	51.671	85.885	403.215	6214	52.024	3393	48.522	87.054	408.706

Sample	**20 MPa**						**10 MPa**					
	Vp	**Qp**	**Vs**	**Qs**	**ϱ**	**F**	**Vp**	**Qp**	**Vs**	**Qs**	**ϱ**	**F**
Base Bed 2	4081	60.098	2146	28.761	3.716	17.446	3989	39.334	2081	20.007	3.676	17.257
Base Bed 3	4063	53.671	2150	34.889	3.609	16.945	4011	39.224	2103	21.760	3.753	17.620
Base Bed 4	4053	27.521	2157	24.810	3.364	15.791	3982	21.901	2110	19.958	3.366	15.803
BWB 2	4047	35.554	2120	20.320	3.792	17.800	3946	26.269	2043	16.582	3.755	17.631

BWB 3	4090	33.803	2182	23.846	4.134	19.407	3993	23.808	2110	16.651	3.957	18.577	4132	7.604	2366	10.601	5.330	25.025	4056	7.448
BWB 4	4176	41.199	2248	22.510	3.669	17.226	4160	42.862	2235	25.396	3.587	16.842	4364	16.133	2549	13.471	6.249	29.336	4395	12.445
Pond Free Stone	4364	74.434	2369	54.162	8.651	40.616	4223	42.902	2289	24.924	8.606	40.404	4531	23.309	2307	16.284	30.286	142.187	4351	13.327
RS08A	3783	16.662	1941	14.935	7.289	34.218	3576	9.444	1790	9.046	6.926	32.514	4564	18.263	2547	23.992	47.480	222.908	4767	11.024
RS08B	3459	12.153	1620	11.041	6.374	29.924	3261	9.947	1489	10.206	6.121	28.736	4862	7.959	2332	9.312	28.449	133.564	4021	5.434
RS08C	4389	8.224	2378	9.122	13.098	61.493	4226	7.279	2146	9.172	12.365	58.052	4225	16.649	2486	12.300	39.508	185.484	4625	10.855
WB 2	4078	26.266	2318	25.541	4.899	23.000	3998	22.095	2288	20.292	4.840	22.721	4319	19.753	2281	33.076	17.414	81.757	3918	7.273
S-39400	5248	45.785	2649	15.645	184.342	865.455	5176	26.017	2598	10.480	154.894	727.202	3624	12.052	2334	10.462	24.537	115.198	3435	7.793
S-39415	3624	12.052	2334	10.462	24.537	115.198	3435	7.793	2196	9.669	25.376	119.137	5113	27.443	2657	18.560	39.582	185.832	4942	16.532
S-39433	5113	27.443	2657	18.560	39.582	185.832	4942	16.532	2629	15.113	43.580	204.603	4124	7.387	2182	21.521	22.591	106.063	3964	5.566
S-39437	4124	7.387	2182	21.521	22.591	106.063	3964	5.566	2096	19.092	21.391	100.429	3961	18.407	2347	17.308	11.750	55.162	3779	12.142
S-39438	3961	18.407	2347	17.308	11.750	55.162	3779	12.142	2023	15.383	10.647	49.986	4319	19.753	2281	33.076	17.414	81.757	3918	7.273
S-39440	4319	19.753	2281	33.076	17.414	81.757	3918	7.273	2137	13.824	15.379	72.200	4862	16.649	2486	12.300	39.508	185.484	4625	10.855
S-39446	4862	16.649	2486	12.300	39.508	185.484	4625	10.855	2373	7.735	34.354	161.286	4225	7.959	2332	9.312	28.449	133.564	4021	5.434
S-39448	4225	7.959	2332	9.312	28.449	133.564	4021	5.434	2242	9.089	25.078	117.737	4939	18.263	2547	23.992	47.480	222.908	4767	11.024
S-39454	4939	18.263	2547	23.992	47.480	222.908	4767	11.024	2379	16.609	39.393	184.944	4564	23.309	2307	16.284	30.286	142.187	4351	13.327
S-39464	4564	23.309	2307	16.284	30.286	142.187	4351	13.327	2234	12.218	27.466	128.947	4531	16.133	2549	13.471	6.249	29.336	4395	12.445
Alg 1.1	4531	16.133	2549	13.471	6.249	29.336	4395	12.445	2428	13.129	5.875	27.580	4132	7.604	2366	10.601	5.330	25.025	4056	7.448
Alg 1.3	4132	7.604	2366	10.601	5.330	25.025	4056	7.448	2360	8.721	5.204	24.431	4531	16.133	2549	13.471	6.249	29.336	4395	12.445

Bio 1.1	4732	23.071	2567	19.442	66.410	311.785	4653	18.091	2530	17.598	64.052	300.712	
Bio 2.2	5356	4.981	2557	12.028	8.708	40.884	5354	5.917	2340	8.507	8.448	39.664	
BM 1	5843	26.730	3205	14.648	46.927	220.315	5761	21.276	3150	14.321	43.715	205.235	
BM 2	5717	19.552	3173	8.256	32.070	150.562	5602	14.812	2986	10.686	29.590	138.922	
BM 3	6182	45.552	3433	36.036	70.867	332.709	6118	36.800	3388	40.602	65.148	305.859	
BM 4	6265	18.822	3472	23.538	69.265	325.188	6203	16.431	3448	21.101	61.881	290.521	
BV 2	4869	23.992	2764	18.578	11.722	55.031	4787	21.056	2699	19.012	10.808	50.740	
GRN 1	6543	56.593	3555	67.422	150.990	708.873	6466	43.906	3500	41.345	125.060	587.136	
GRN 2	5478	80.862	3062	33.884	21.847	102.568	5392	50.379	3006	23.249	20.828	97.784	
GRN 3	5381	41.736	2943	22.443	17.858	83.840	5295	29.473	2901	19.304	17.449	81.920	
GRN 4	4790	16.264	2672	16.954	8.322	39.071	4703	13.743	2621	18.488	8.092	37.989	
S-39456	5750	19.590	3215	21.133	18.505	86.878	5427	7.430	3163	17.913	15.863	74.476	
S-39457	6147	35.427	3366	36.883	80.137	376.228	6053	24.206	3297	16.178	61.566	289.041	